Electronic Supplementary Material (ESI) for Energy & Environmental Science.
This journal is © The Royal Society of Chemistry 2024

Supplementary information for

Revisiting the unified principle for the single-atom electrocatalysts in sulfur reduction reaction: from liquid to solid-state electrolytes

Jiadong Shen[†], Ziwei Liang[†], Tengteng Gu[†], Zhaoyu Sun, Yiwen Wu, Xiaoqin Liu, Junhao Liu, Xiuying Zhang, Jiangwen Liu, Lei Shen[*], Min Zhu and Jun Liu[*]

*Corresponding author. Email: shenlei@nus.edu.sg; msjliu@scut.edu.cn

Supplementary noted 1: Constructions of Calculations.

The Hamiltonian of *d-p* pairs

For the Li_2S_x-TMNCs adsorption, the corresponding *d-p* Hamiltonian between the TMs and N is: where H_{dp} stands for the *d-p* hybridization and H_{pp} for the inter-nitrogen *p-p* hopping, H_{so} is the spin-orbit coupling, and H_{diag} is the diagonal part of kinetic energy. H^{d}_{int} and H^{p}_{int} stand for intra-atomic Coulomb interactions at M and N ions, respectively, respectively. *i*, *j*, *u*, and *v* are site; $t_{i\mu;jv}$ and $t_{m\alpha,jv}$ are assumed to be non-zero only for nearest neighbor TM and N *d-p* pairs. Because there are no heavy metals in the system, the H_{soc} is negligible. From the PDOS, there is non-binding states near E_{F} and no overlap between *p* states of Fe and *p* states of N. Thus, the H^{d}_{int} and H^{p}_{int} are negeligible.

$$H_{Fe-N} = H_{pd} + H_{pp} + H_{SOC} + H_{diag} + H^{d}_{int} + H^{p}_{int} \quad (1)$$

$$H_{dp} = \sum_{\{m\alpha;jv\},\sigma} (t_{m\alpha,jv} d^{*}_{m\alpha,\sigma} p_{jv,\sigma} + H.c.) \quad (2)$$

$$H_{pp} = \sum_{\{i\mu;jv\},\sigma} (t_{i\mu;jv} d^{*}_{i\mu,\sigma} + H.c.) \quad (3)$$

Computational details of DFT calculations

The DFT calculations were performed by the Vienna Ab-initio Simulation Package (VASP) and used the projector augmented wave (PAW) method to describe the behavior of electronics[1,2]. The exchange-correlation energy was treated using the generalized gradient approximation (GGA) and the Perdew-Burke-Ernzerhof (PBE) functional[3]. Based on the convergence testing results, the kinetic energy cutoff of 985 eV and auto k-point mesh of 4×4×1 were used for the TMNCs surfaces and the corresponding Li_2S_x-TMNCs adsorption models. And considering the computational costs and the accuracy of convergence, the energy cutoff of 520 eV and k-points of 3×3×1 were used for the four-layers $Fe_3C(221)$ surfaces and the corresponding $Fe_3C(221)$-Li_2S_x adsorption models. A vacuum separation over 20 Å was employed to eliminate interactions between two adjacent unit cells. The DFT-D3 correction method was adopted to calculate the binding energy of Li_2S_x species on G/N_4C/TMNCs surfaces for describing the weak interaction of van der Waals forces[4]. The corresponding binding energy was calculated as follows:

$$E_{ad} = E_{total} - E_{slab} - E_{S8/Li2Sx} \quad (4)$$

The E_{ad}, E_{total}, E_{slab}, and $E_{S8/Li2Sx}$ are binding energy, the total energy of adsorption models, the energy of slabs, and the energy of S_8/Li_2S_x species, respectively. The energy and forces convergence criterion for structural optimization is 10^{-7} eV and 0.01 eV $Å^{-1}$, respectively. The Gibbs free energy is calculated according to the follow's equation:

$$G = U - TS = E_{DFT} + ZPE + \int_0^T C_p dT - TS \quad (5)$$

ZPE is the zero-point energy and $\int_0^T C_p dT$ is the enthalpic temperature correction. The climbing-image nudged elastic band (Cl-NEB) method[5] was employed to calculate the energy barriers of Li_2S decomposition on TMNCs and TMBs (Co(111), Ni(111), CoNi(111), and $Fe_3C(221)$) surfaces. The structure relaxation was continued until the forces on all atoms converged to less than 0.02 eV/Å. The visualization of the model is done using VESTA software (ver. 3.4.0, 64-bit Edition)[6], and the processing of Gibbs

free energy is performed in VASPKIT software (Version: 1.20 beta0) [7]. For describing the Coulomb interaction of *d* electrons in VN4C, CrN4C, MnN_4C, FeN_4C, CoN_4C, and NiN4C, the Hubbard-U parameters for Mn, Fe, and Co calculations were set 3.25, 3.7, 3.9, 5.3, 3.32, and 6.2, respectively[8].The *d*/*p* band center was calculated by the following equation[9]:

$$\varepsilon_{d/p} = \frac{\int_{-\infty}^{\infty} n_{p/d}(\varepsilon)\varepsilon \, d\varepsilon}{\int_{-\infty}^{\infty} n_{p/d}(\varepsilon) d\varepsilon} \tag{6}$$

The λ can be approximate calculated by the following equation:

$$\lambda = \sum_{\{m\alpha;jv\},\sigma} \left(t_{m\alpha,jv} d^{*}_{m\alpha,\sigma} p_{jv,\sigma} + H.c.\right) \approx \varepsilon_d/\varepsilon_p \tag{7}$$

The two-dimensional active volcano map is drawn using the Bell–Evans–Polanyi principle (BEP)[10] scaling relationship between the energy barriers for the conversion of $Li_2S_6 \rightarrow Li_2S_4$ and $Li_2S_4 \rightarrow Li_2S$ and the corresponding adsorption energies of Li_2S_4 (G_{ads}^{Li2S4}) and Li_2S_2 (G_{ads}^{Li2S2}).

The *ab-initio* molecular dynamics (AIMD) calculations. The AIMD simulations were performed using a modified version of the mixed Gaussian and plane-wave code (CP2K), particularly the Quickstep algorithm[10,11]. In CP2K, the core electrons and nuclei are represented using the GTH norm-conserving pseudopotential[12]. We employed the double–zeta (ζ) Gaussian basis set plus polarization (DZVP)[13] and a 300 Ry (1 Ry ≈ 13.6 eV) plane-wave cutoff with a relative cutoff of 60 Ry. We employed the Grimme DFT-D3 method to account for dispersion interactions, reproducing the C-

C pair potential. The exchange-correlation interactions were taken into account by the PADE functional[14]. Born-Oppenheimer molecular dynamics simulations have been performed at the same level of theory used for geometry optimizations[15]. The convergence criterion for the self-consistent field method (SCF) energy was 1×10^{-4} eV. Here, the temperature begins with 290 K in the constant–temperature and constant-volume AIMD simulations to mimic the ambient conditions (NVE ensemble). The time step is 1.0 fs, all the systems were pre-equilibrated for 5 ps, and the simulation time is more than 20 ps for each system. The calculations used the orbital transformation (OT) method to accelerate the speed of simulations. Visualization of molecular motion is achieved by using VMD 1.9.3 software[16].

Machine learning algorithms assist in creating descriptors (quadratic polynomial fitting & SISSO). Initially, 73 sets of data (3*d* / 4*d* / 5*d*, including models under different crystal field orbitals) calculated by high-throughput DFT were used as training data for descriptor creation. The quadratic polynomial was directly obtained through the linear regression model of quadratic polynomials in the "sklearn" Python package[17]. The input features include: ε_d / ε_p, Δd, ΔE_{ion}, M_{ratio}, and R_{ratio}; where β_0, β_1, β_2, and ε are the coefficients corresponding to the quadratic polynomial fitting. Δd denotes the vertical nearest distance between metal and non-metal atoms; the electronic structural information of the metal is characterized by the metal's first ionization energy ΔE_{ion}; the mole mass ratio and atomic radius ratio between metal and non-metal atoms are

represented by M_{ratio} and R_{ratio}, respectively. Additionally, the same data set and input features were used to fit the descriptor using the "Sure Independence Screening and Sparsifying Operator" (SISSO)[18], with the calculation rules between descriptors limited to “+” and “×”.

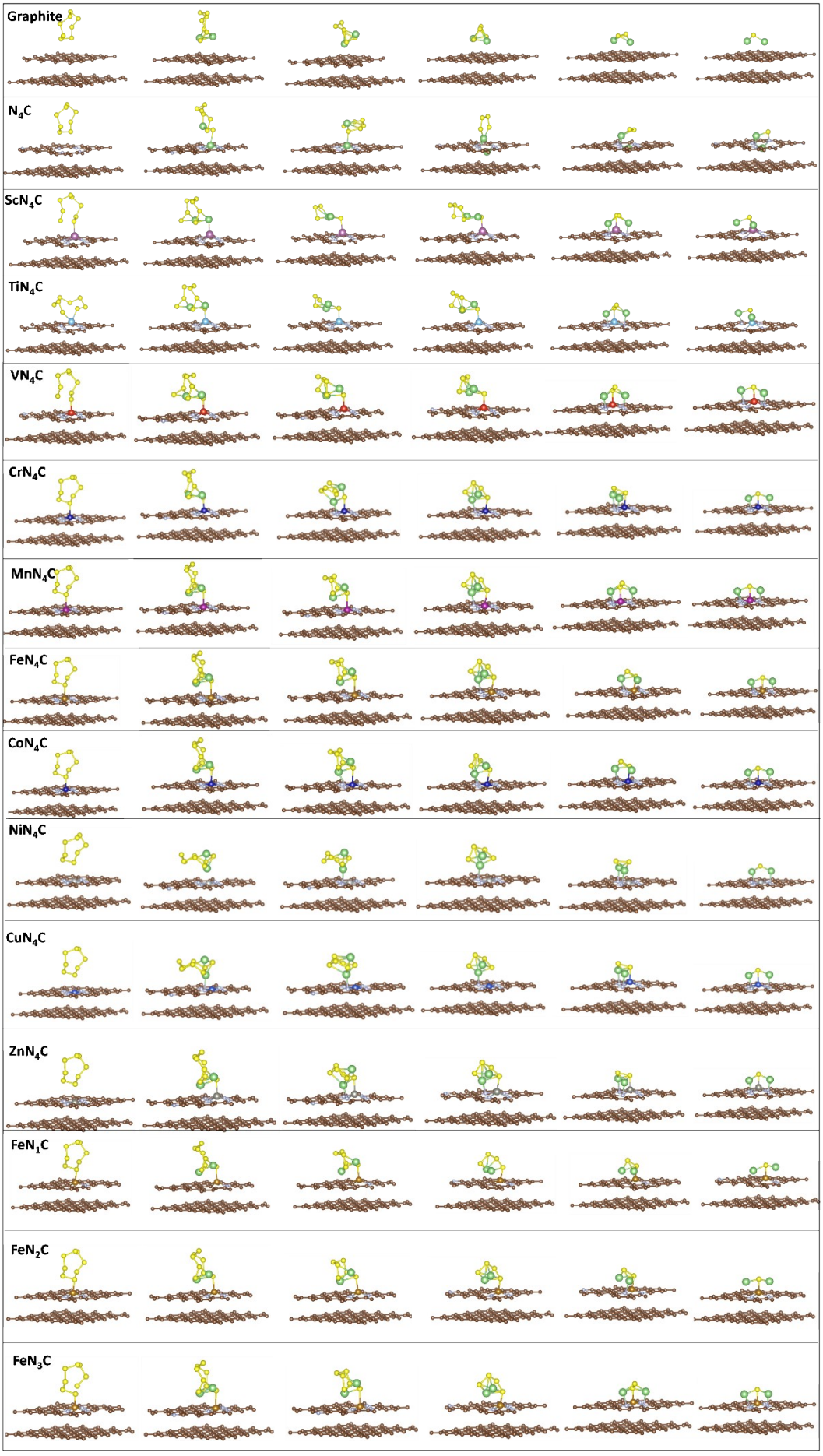
Graphite
N_4C
ScN_4C
TiN_4C
VN_4C
CrN_4C
MnN_4C
FeN_4C
CoN_4C
NiN_4C
CuN_4C
ZnN_4C
FeN_1C
FeN_2C
FeN_3C

Supplementary Fig. 1 The geometry configurations of optimized Li_2S_x-G/N_4C/TMNCs adsorption models (G: Graphite; TMNCs: ScN_4C, TiN_4C, VN_4C, CrN4C, MnN_4C, FeN_4C, CoN_4C, NiN_4C, CuN_4C, ZnN_4C, FeN_1C, FeN_2C, and FeN_3C).

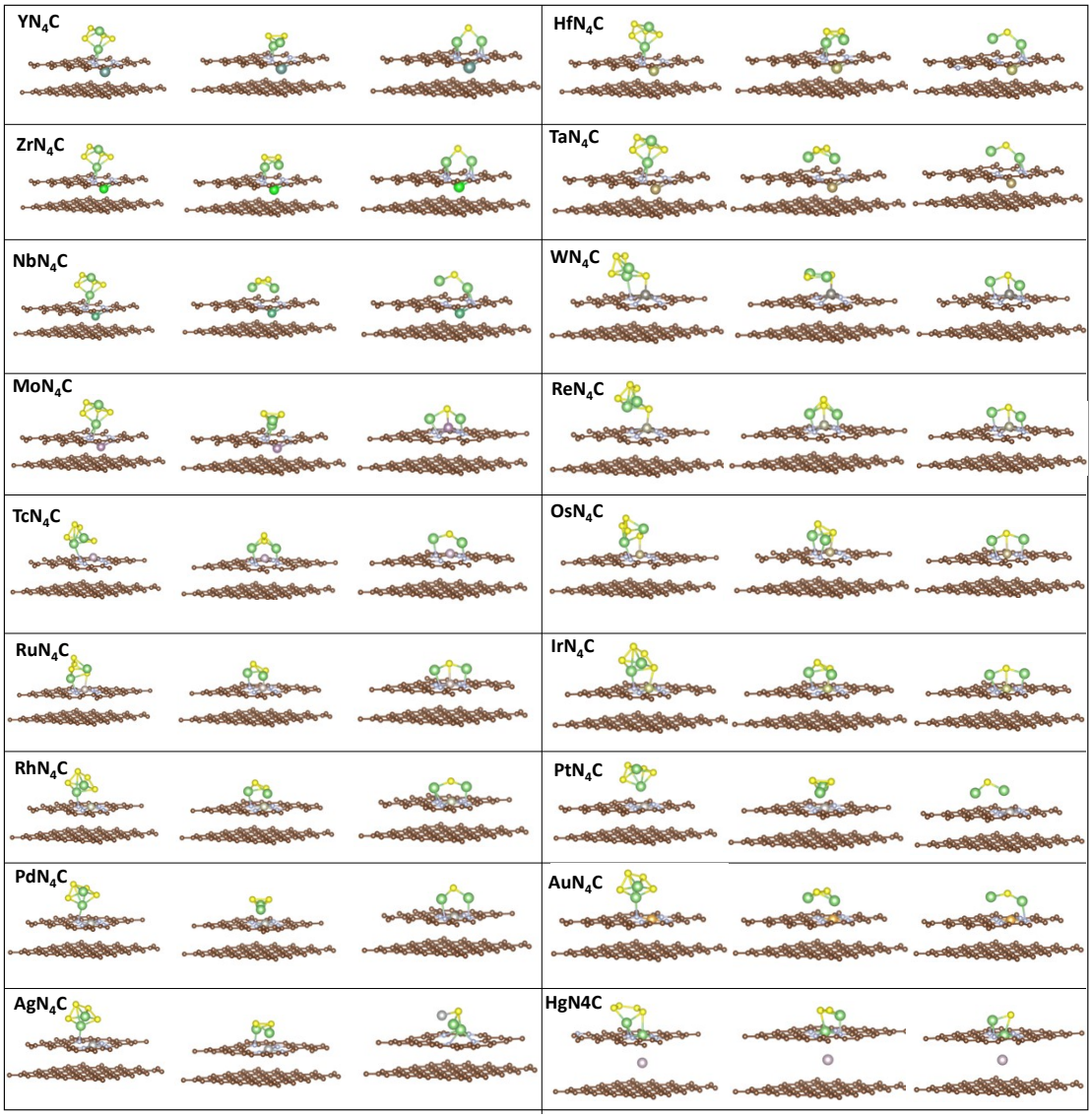

Supplementary Fig. 2 The geometry configurations of optimized Li_2S_x-G/N_4C/TMNCs adsorption models (G: Graphite; TMNCs: ScN_4C, TiN_4C, VN_4C, MnN_4C, FeN_4C, CoN_4C, ZnN_4C, FeN_1C, FeN_2C, and FeN_3C).

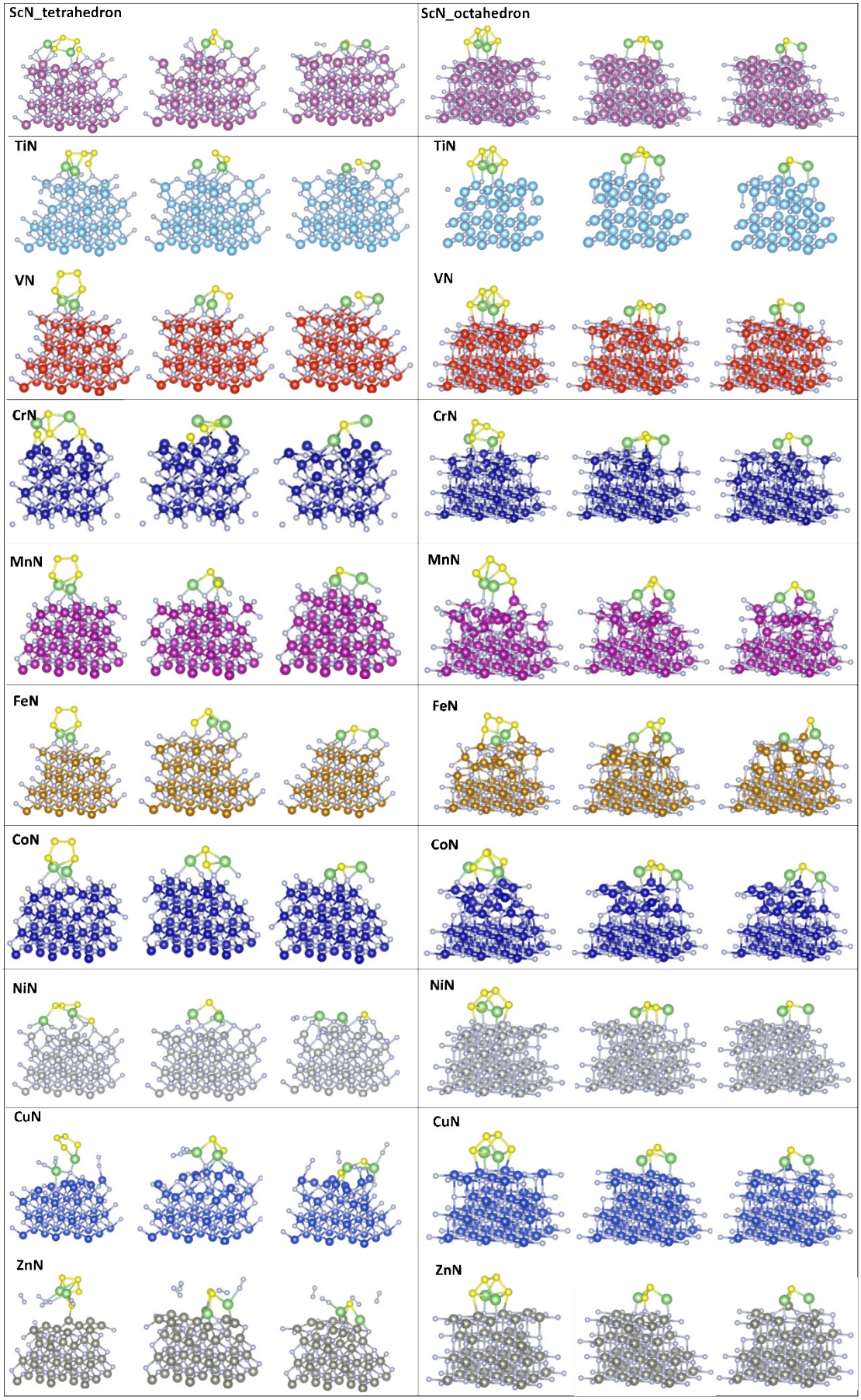
ScN_tetrahedron
ScN_octahedron
TiN
TiN
VN
VN
CrN
CrN
MnN
MnN
FeN
FeN
CoN
CoN
NiN
NiN
CuN
CuN
ZnN
ZnN

Supplementary Fig. 3 The geometry configurations of optimized Li_2S_x-G/N_4C/TMNCs adsorption models (G: Graphite; TMNCs: ScN_4C, TiN_4C, VN_4C, MnN_4C, FeN_4C, CoN_4C, ZnN_4C, FeN_1C, FeN_2C, and FeN_3C).

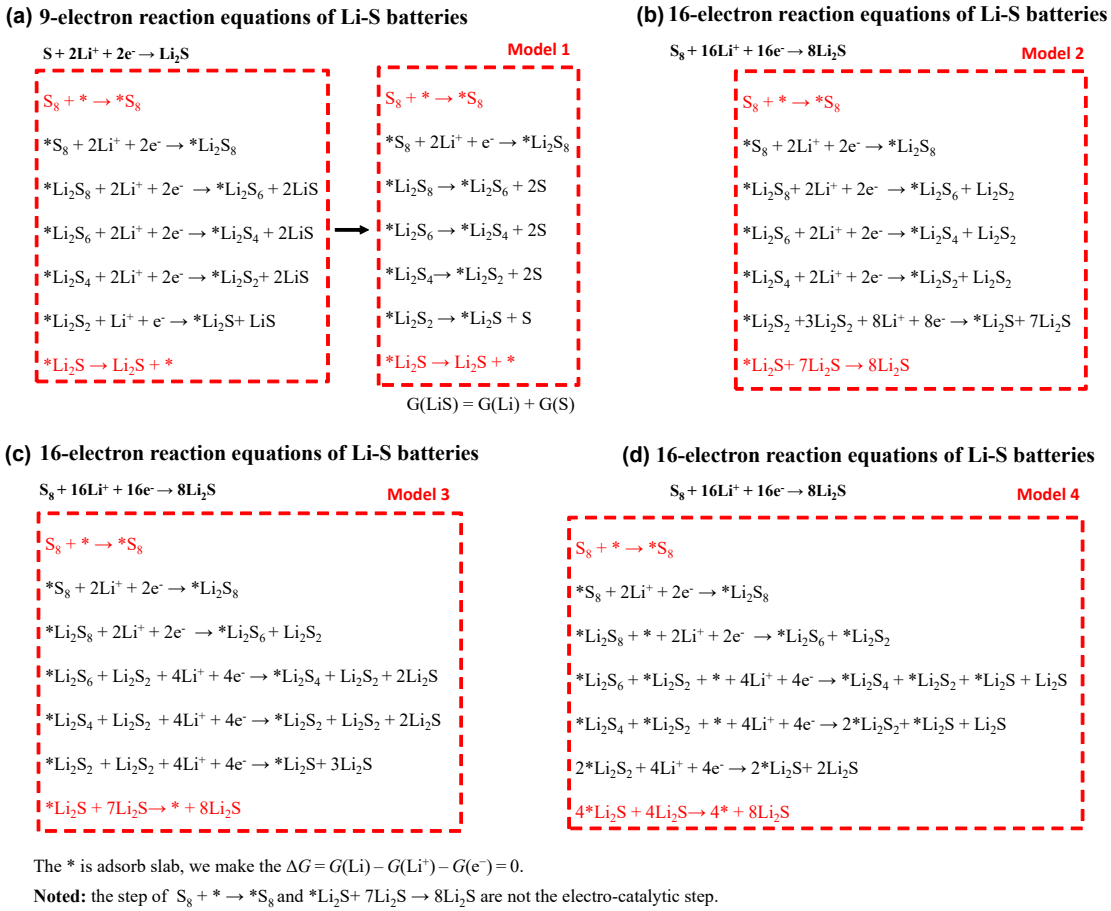

Supplementary Fig. 4 The reaction pathway of SRR. **(a)** Model 1 is the 9-electron reaction, and **(b-d)** model 2-4 are 16 electron reaction.

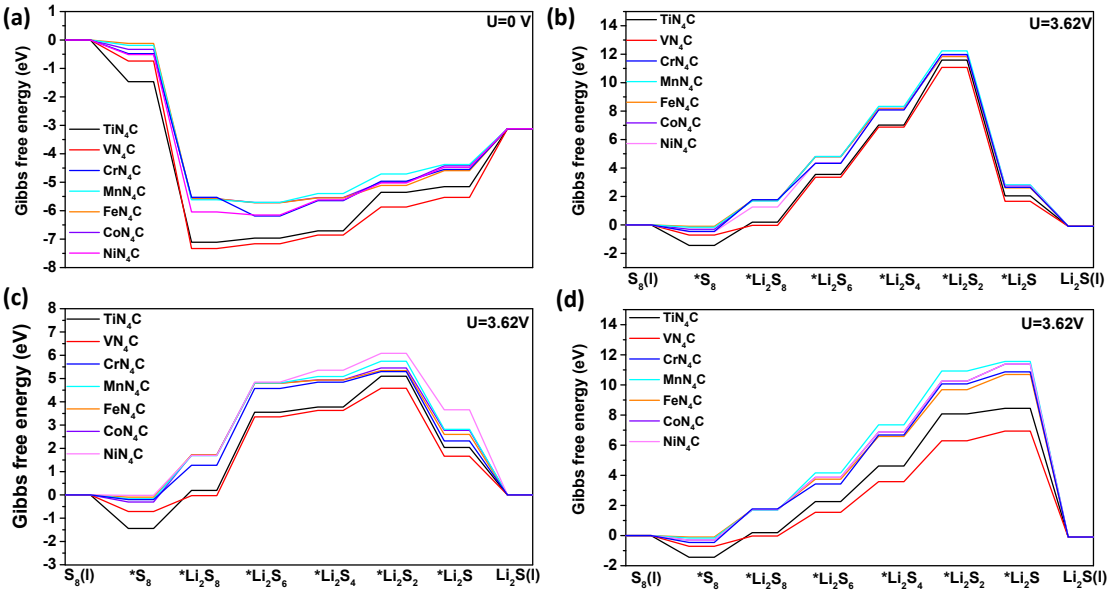

Supplementary Fig. 5 The Gibbs free energy calculation results of SRR on the TMNCs based on (**a)** model 1; (**b)** model 2; (**c)** model 3; and (**d)** model 4. **Noted:** the externally applied voltage for (**b-d)** is 3.62V.

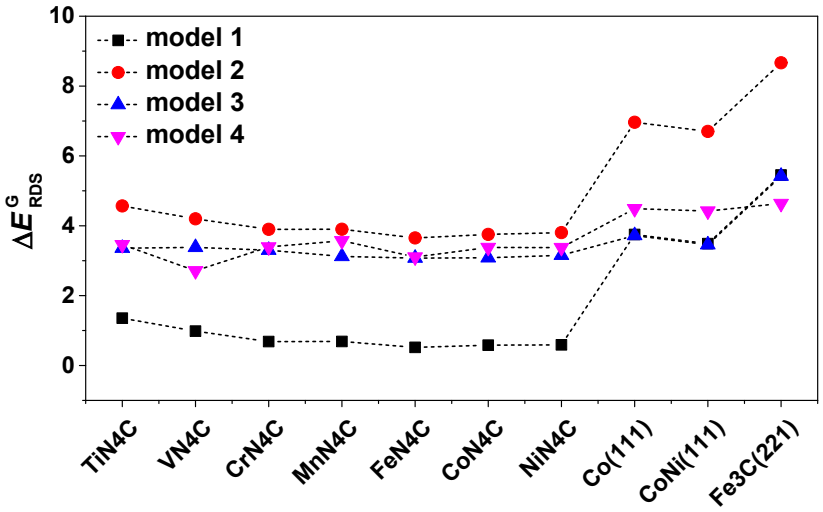

Supplementary Fig. 6 The ΔG_{RDS} results of SRR in 4 models: without (**a**) and with (**b**) the externally applied voltage of 3.62 V. (The RDS data of Li_2S_x-Co(111), Li_2S_x-CoNi(111) are cited from Ref.19[19]

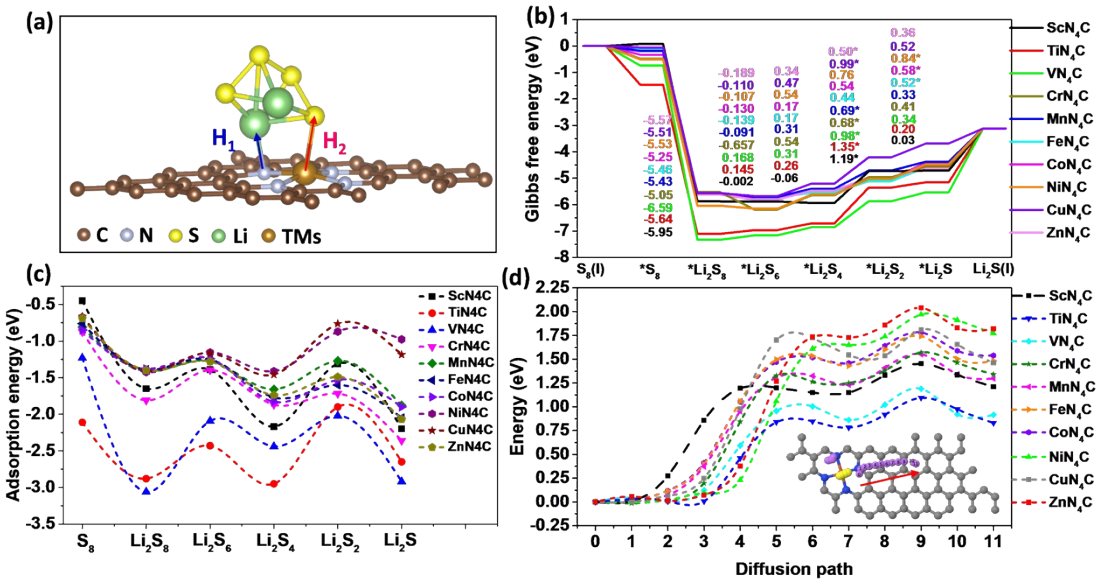

Supplementary Fig. 7 (a) The main Hamiltonian of optimized Li_2S_x-TMNCs adsorption model (H1: Hamiltonian of N and Li; H2: Hamiltonian of metal and sulfur). (**b**) The ΔE_{RDS}^{G} of the reduction reaction of Li_2S_x (x = 1, 2, 4, 6, and 8) on the surface of TMNCs. **(c)** The adsorption energy of Li_2S_x on TMNC surfaces (M = Sc, Ti, V, Cr, Mn, Fe, Co, Ni, Cu, and Zn); (**d**) The decomposition energy barrier of Li_2S on TMNCs surfaces (the inserts is the decomposition path of Li_2S).

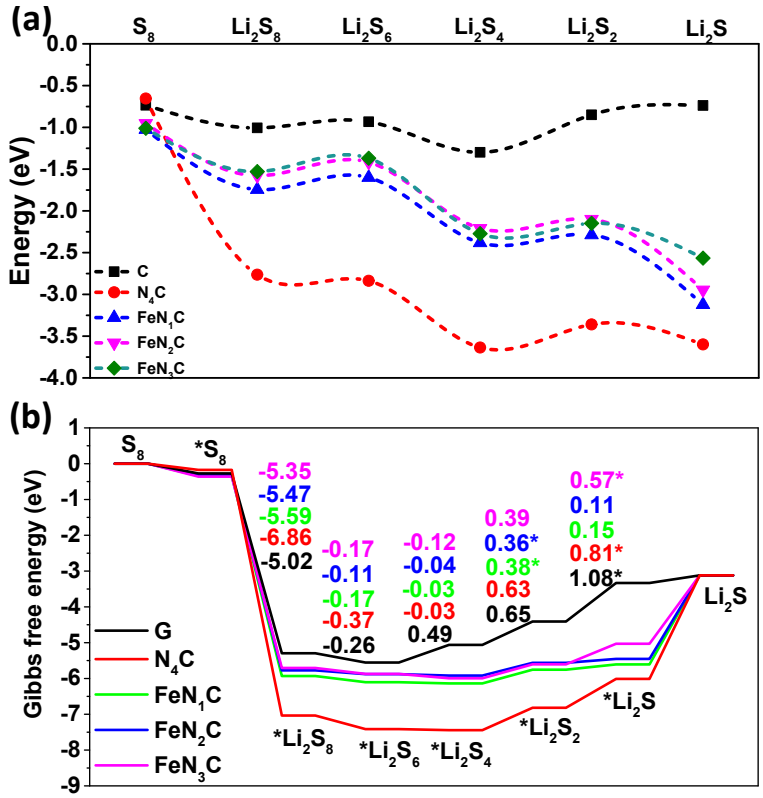

Supplementary Fig. 8 (a, b) The adsorption energy (**a**) and the corresponding Gibbs free energy change (**b**) of S_8 and LPSs on graphite, N_4C, FeN_xC (x = 1, 2, 3 and 4) surfaces.

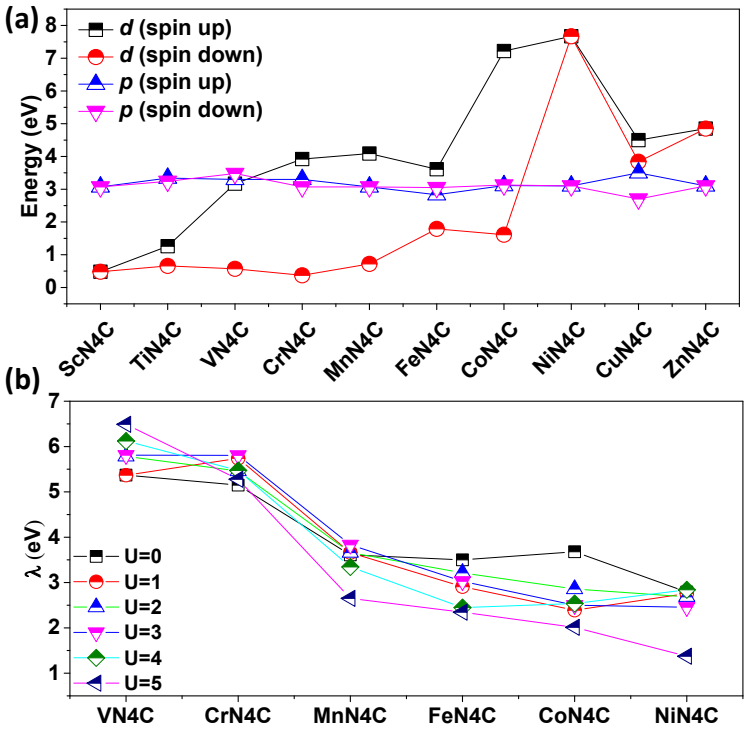

Supplementary Fig. 9 (**a**) The electrons' number of *d* band and *p* band of TMNCs surfaces. The integrating range is from -25 eV to Fermi-level (0 eV). (**b**) The λ data of VN_4C, CrN_4C, MnN_4C, FeN_4C, CoN_4C, and NiN_4C surface with different Hubbard-U data.

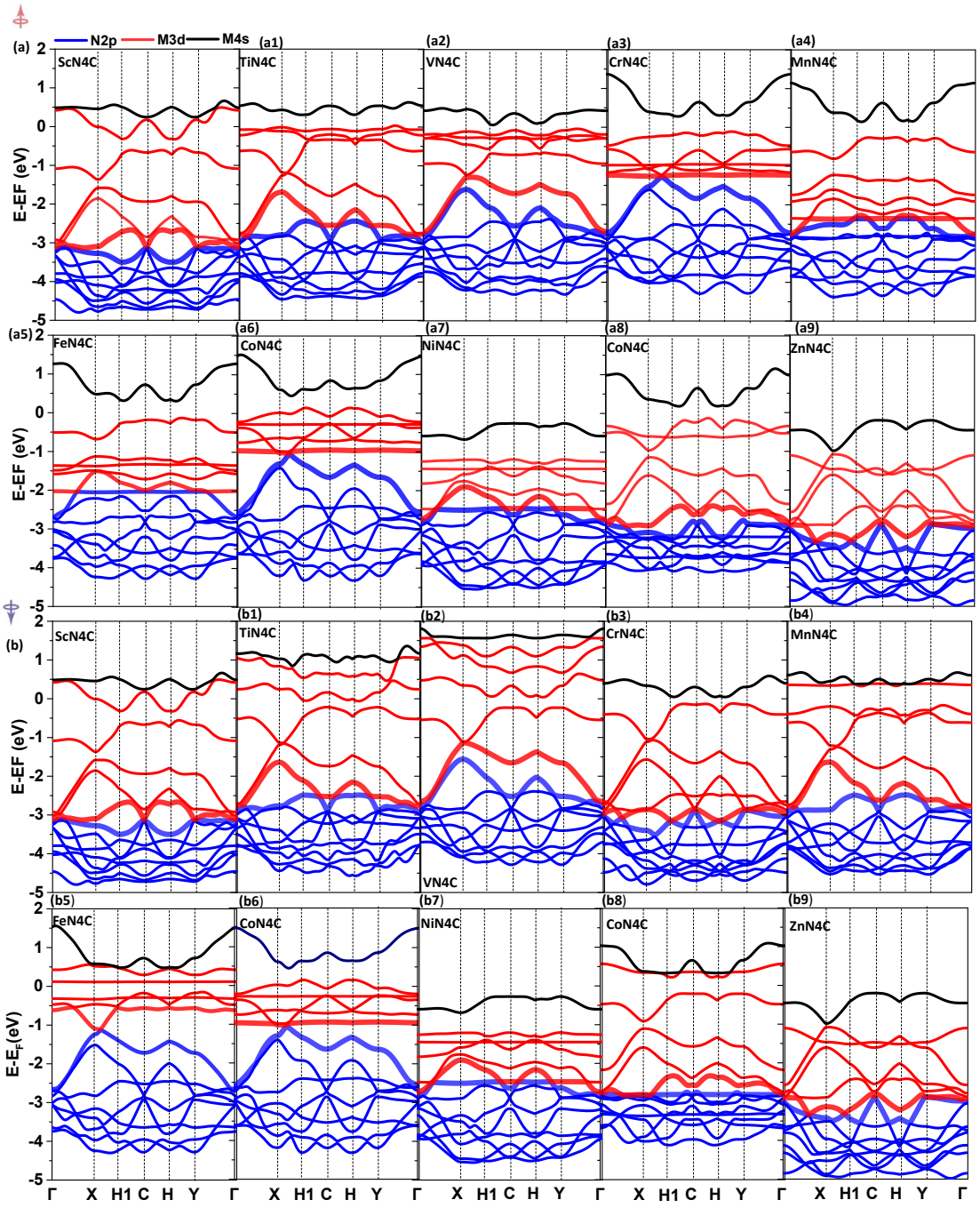

Supplementary Fig. 10 Band structure of TMNCs model with spin polarization about spin up (**a-a9**) and spin down (**b-b9**) directions (The energy band is obtained from the tight-binding model.)

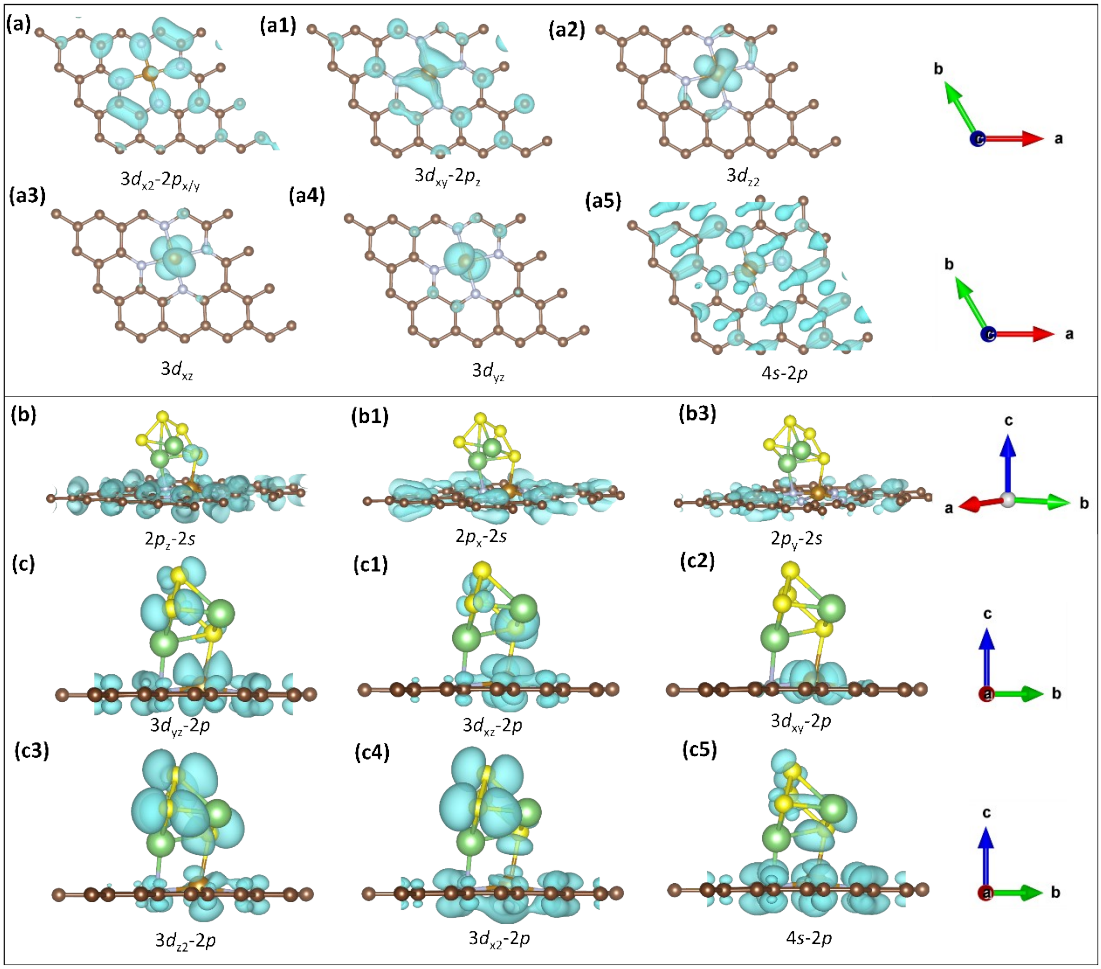

Supplementary Fig. 11 Wave function analysis of Fe-N, N-Li_2S_4, and Fe-Li_2S_4 in the FeN_4C system. (a-a5) The interactions of 3*d*-2*p*/4*s*-2*p* wave function between the Fe and N atom. (**b-b3)** The interactions of 2*p*-2*s* wave function between the N and Li atom; **(c-c5)** the interactions of 3*d*-2*p*/4*s*-2*p* wave function between the Fe and S atom.

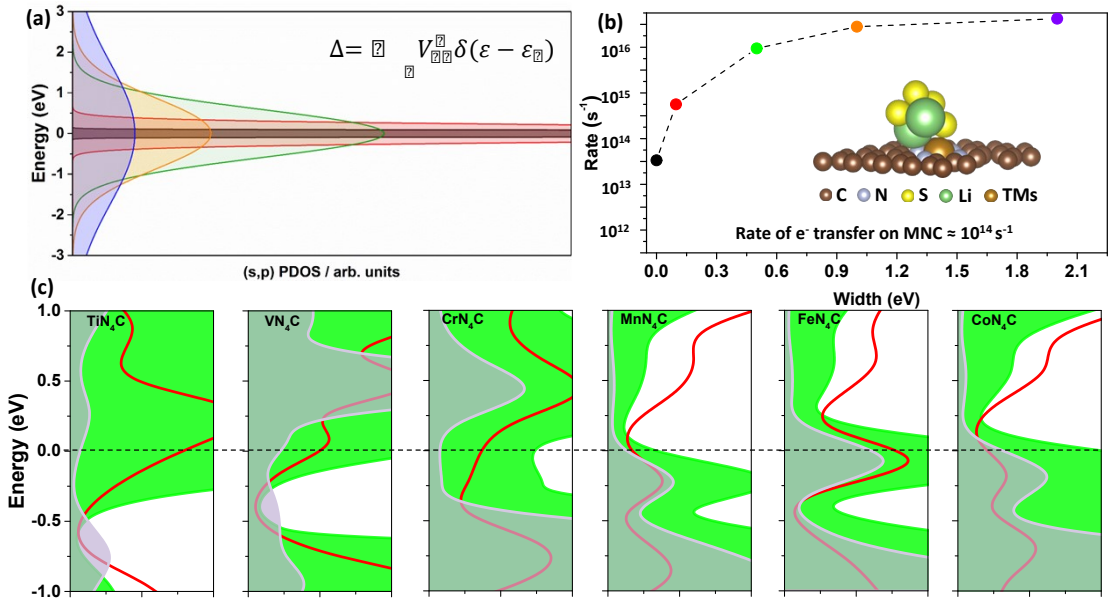

Supplementary Fig. 12 (a, b) The idealized Lorentzian peaks with different widths (**a**) and the corresponding rate of electron hopping rate[20] (**b**). (**c**) The DOS of Li_2S_4-TMNCs adsorption models; the green pattern is the *d* states of metal atoms, the red line is the *p* states of N atoms, and the purple pattern is the *s*/*p* states for Li_2S_4*.

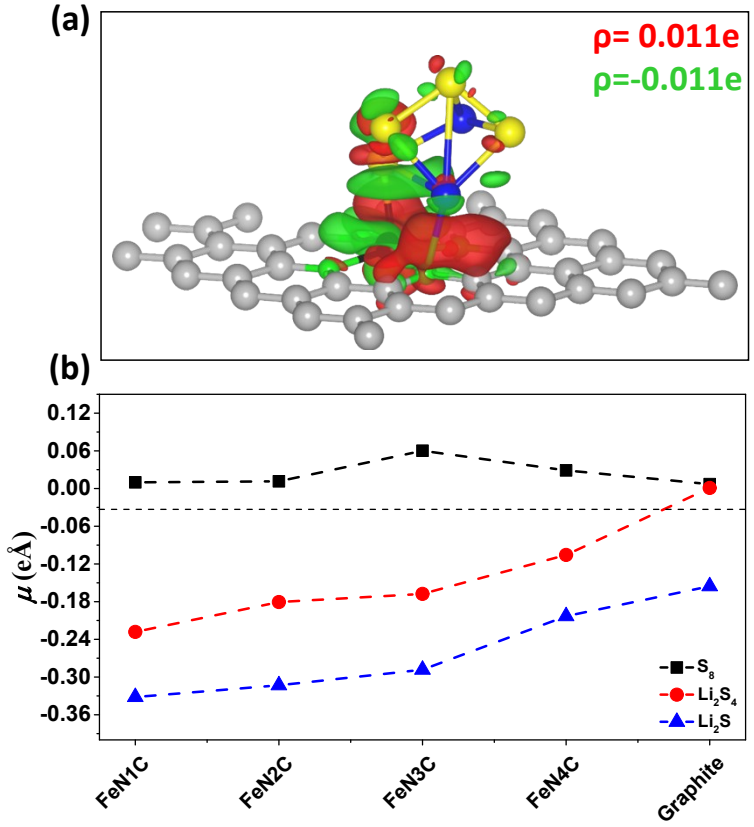

Supplementary Fig. 13 (a) Charge density difference plot of Li_2S_4 adsorbed on FeN_4C surface. **(b)** Vacuum dipole moments of S_8, Li_2S_4 and Li_2S on FeN_1C, FeN_2C, FeN_3C, FeN_4C and Graphite surfaces.

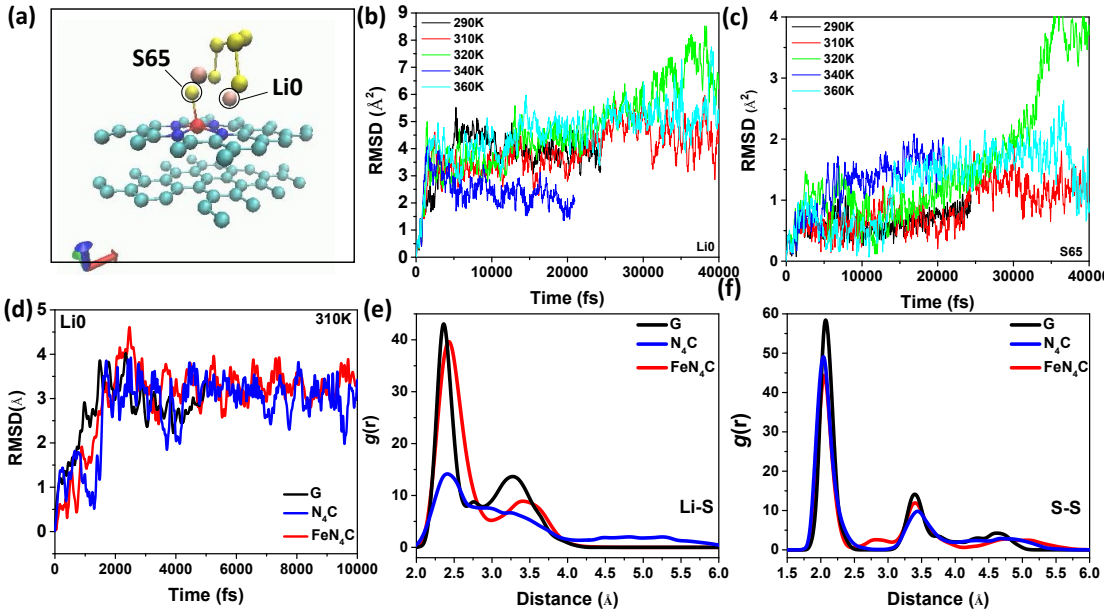

Supplementary Fig. 14 The AIMD results of Li_2S_6-G/N_4C/FeN_4C adsorption models. (a) The initial model of the Li_2S_6-FeN_4C; (**b,c**) the RMSD of Li0 (**b**) and S65 atom (**c**) under 290K, 310K, 320K, 340K, and 360K in the Li_2S_6-FeN_4C model. (**d**) The RMSD curve of Li0 atom and Radial Pair Distribution Function (RDS) of Li-S (**e**) and S-S species (**f**) in Li_2S_6-G/N_4C/FeN_4C adsorption models under 310K.

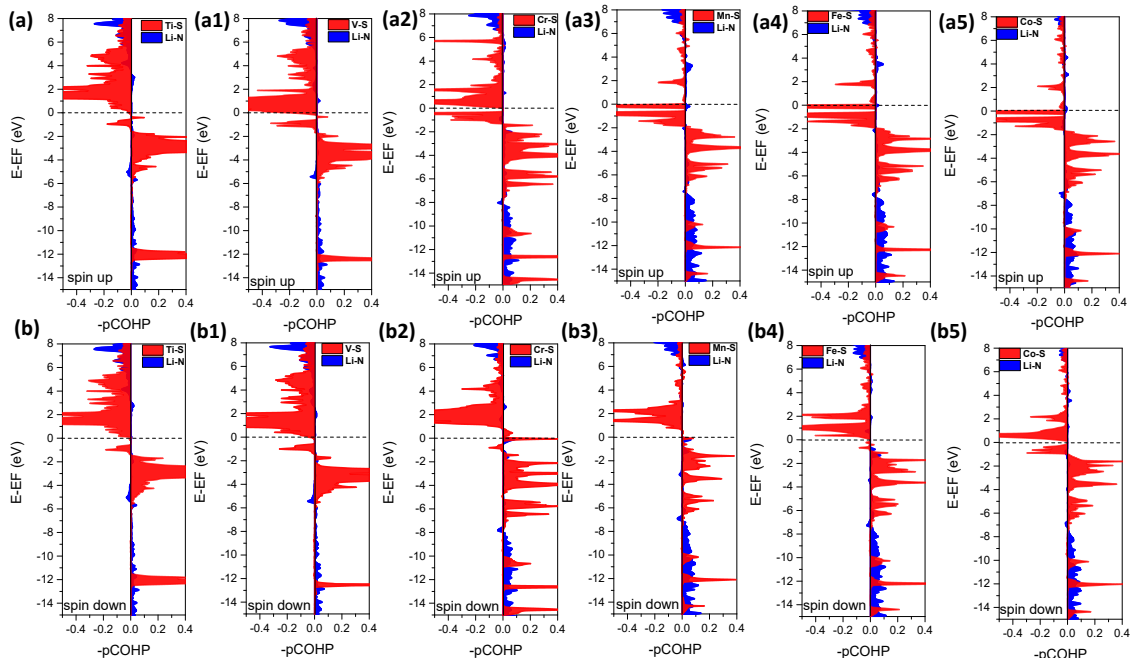

Supplementary Fig. 15 The COHP results of the M-S bond and the Li-N bond calculated based on spin-up (**a-a6)** electrons and spin-down electrons (**b-b6**) in Li_2S_4-TMNCs adsorption models (M = Ti, V, Cr, Mn, Fe, Co, and Ni).

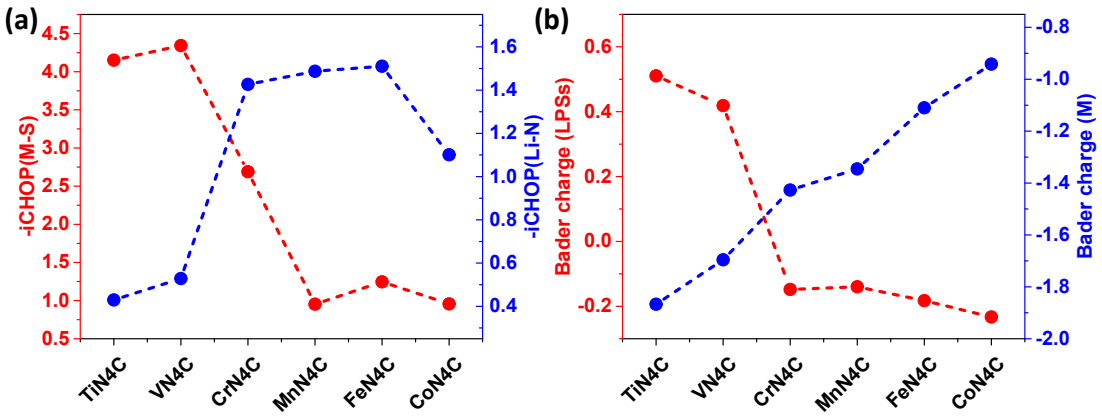

Supplementary Fig. 16 iCOHP and Bader charge transfer results. (a) The iCOHP results of M-S/Li-N bond in Li_2S_4-TMNCs adsorption models. (**b**) The Bader charge transfer results of Li_2S_4 species in corresponding adsorption models.

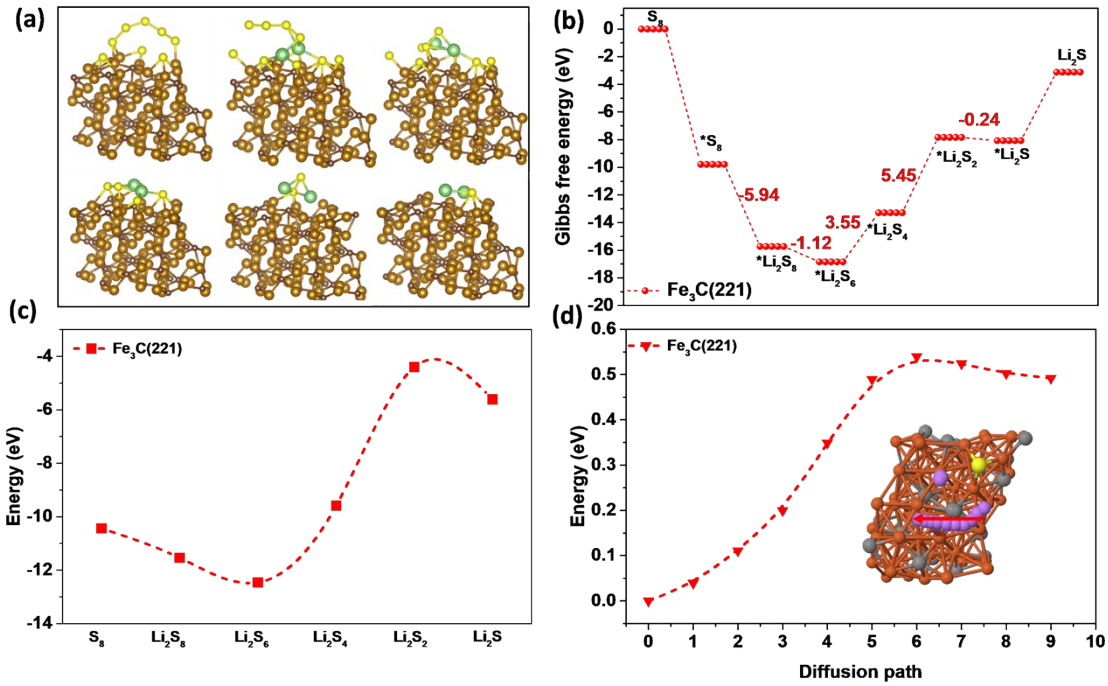

Supplementary Fig. 17 (a) The geometry configurations of optimized LPSs-$Fe_3C(221)$ adsorption models; (**b**) Gibbs Free energy calculation results of LPSs -$Fe_3C(221)$ systems; (**c**) Adsorption energy data of $Fe_3C(221)$ to LPSs. (**d**) The energy barrier of Li_2S decomposition on $Fe_3C(221)$ surfaces (the insert is the pathway of Li_2S decomposition).

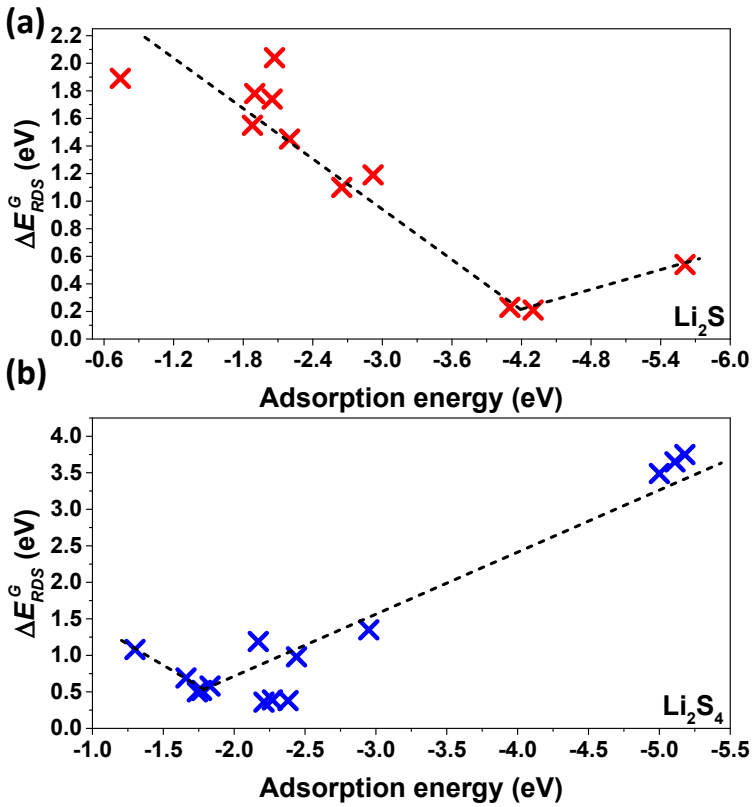

Supplementary Fig. 18 The one-dimensional activity volcano diagram of LPSs' SRR and Li_2S decomposition. (a) The relationship between the binding energy of Li_2S and Li_2S decomposition energy barrier. **(b)** The relationship between the adsorption energy of Li_2S_4 and ΔE^G_{RDS}.

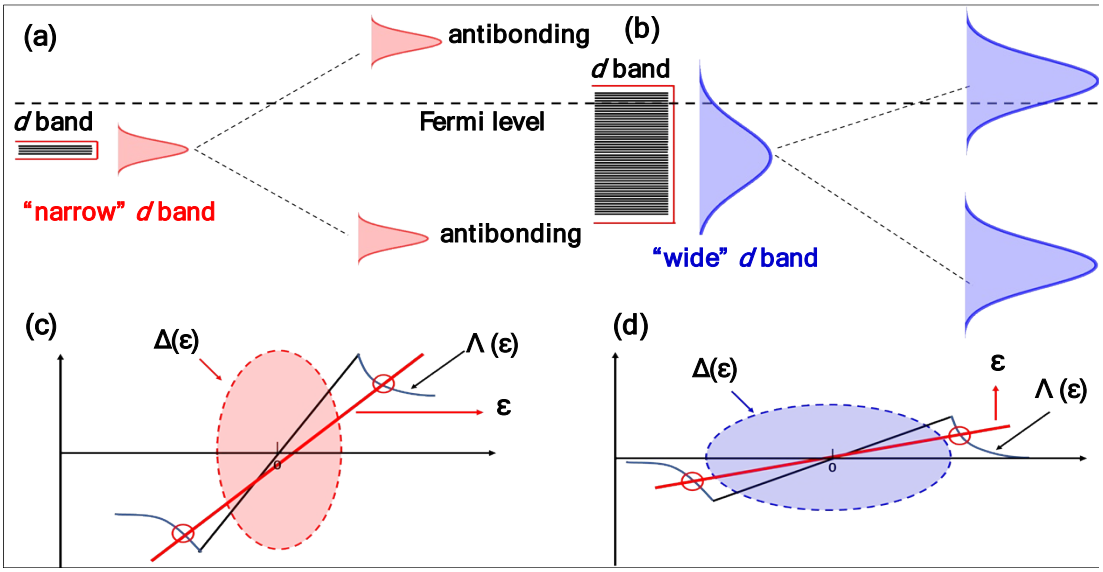

Supplementary Fig. 19 (a,b) Schematic illustration of the interaction between bonding states (*s*/*p* states of Li/S bonding with 4*s* states of transition metals) and narrow (**a**) or broad (**b**) width of 3*d* states for transition metals; (**c**,**d**) the corresponding semielliptical Δ(ε) with Hilbert transform Λ(ε) of narrow (**c**) or broad (**d**) *d* band.

In Supplementary Fig. 16, if the d-p coupling strength is further enhanced, the adsorption strength of catalysts on LPSs will increase. In order to explain this phenomenon, we analyzed the electronic structure of LPSs-TMNCs and LPSs-Fe_3C(221) adsorption models to find the reasons that caused this abnormal situation. Figure 2f shows the DOS of the VN_4C, MnN_4C, FeN_4C, CoN_4C, ZnN_4C, and Fe_3C (221) with the stable Li_2S_4 adsorption configurations, and we found that the width of *d* states of Fe_3C (221) is larger than the TMNCs. We believe that this is due to the fact that the accumulated metal atoms lead to a larger *d* state width of Fe_3C (221), as shown in Supplementary Fig. 17a and 17b. According to the Newns-Anderson adsorption model, as established in Supplementary Fig. 17c and 17d, we can see that the large valence band width endows its higher hybridization ability with the adsorbate. It causes the more significant electrons to transfer, making the enormous binding strength[21]. Subsequently, under conditions of similar atomic coordination environment and with the same grade of adsorption energy for LPSs, our proposed criterion still applies. This has been confirmed in our previous study[22]. and that of Qian[23].

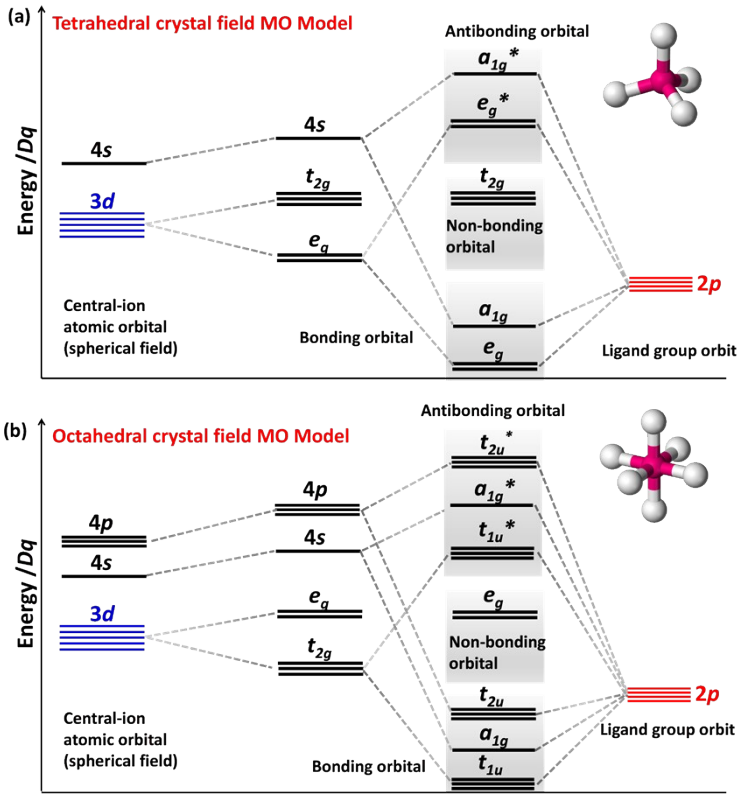

Supplementary Fig. 20 a,b, The energy level splitting diagrams of *d* orbitals for 3*d* metals under tetrahedral (**a**) and octahedral (**b**) crystal fields, along with the molecular orbital diagrams formed with non-metals.

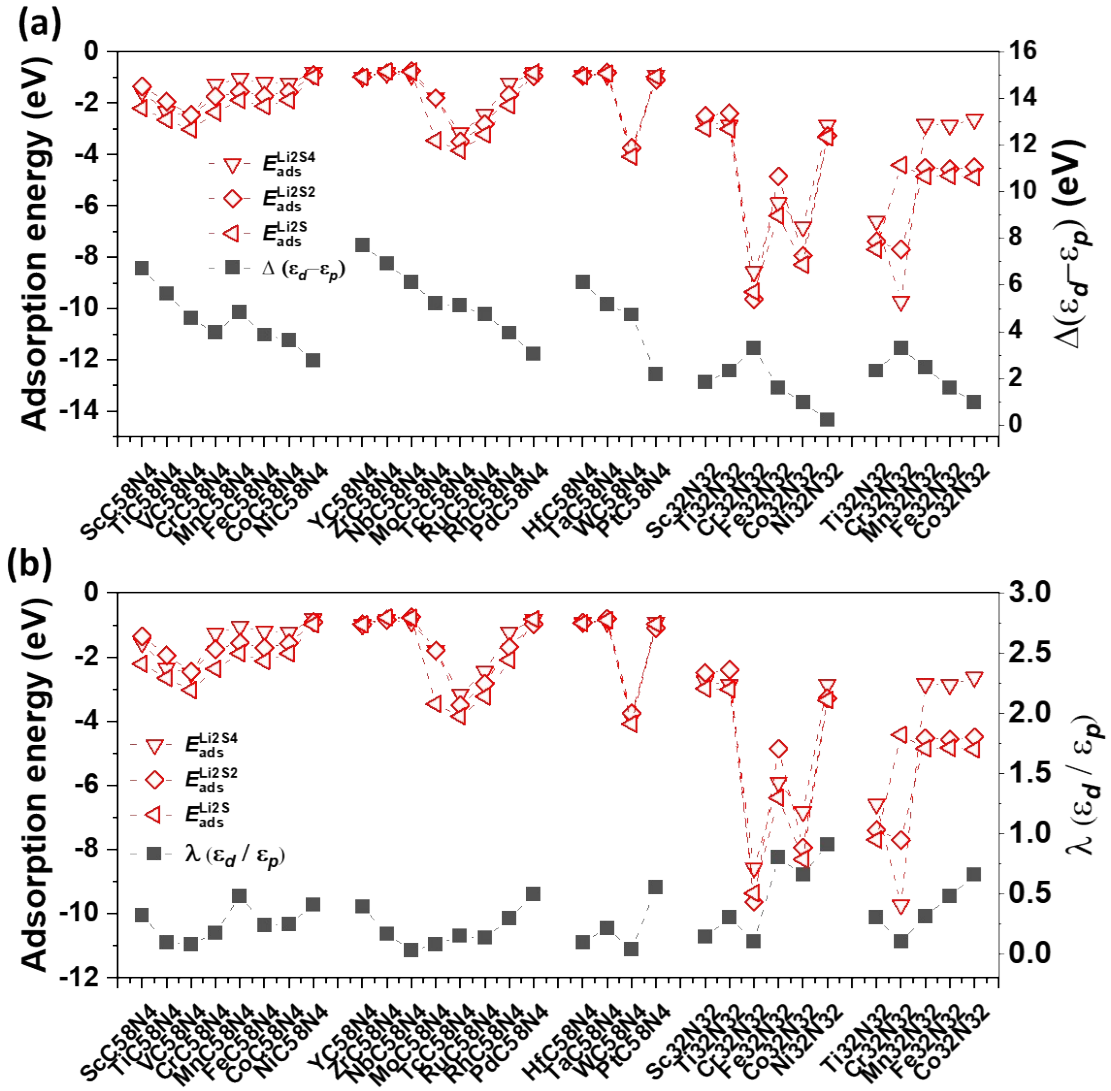

Supplementary Fig. 21 Comparison of E_{ads}^{Li2Sx} (x = 1, 2, and 4) for 3*d*/4*d*/5*d* MNCs and 3*d* MNCs under the influence of tetrahedral/octahedral crystal fields with (a) Δ (ε_d - ε_p) and (b) λ (ε_d / ε_p).

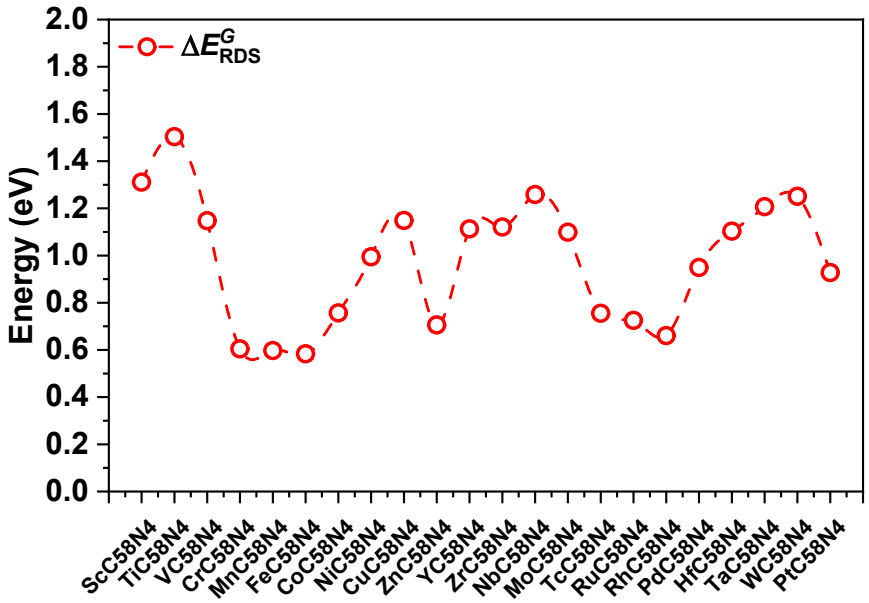

Supplementary Fig. 22 Comparative results of transformation activity for 3d/4d/5d MN_4C-LPSs.

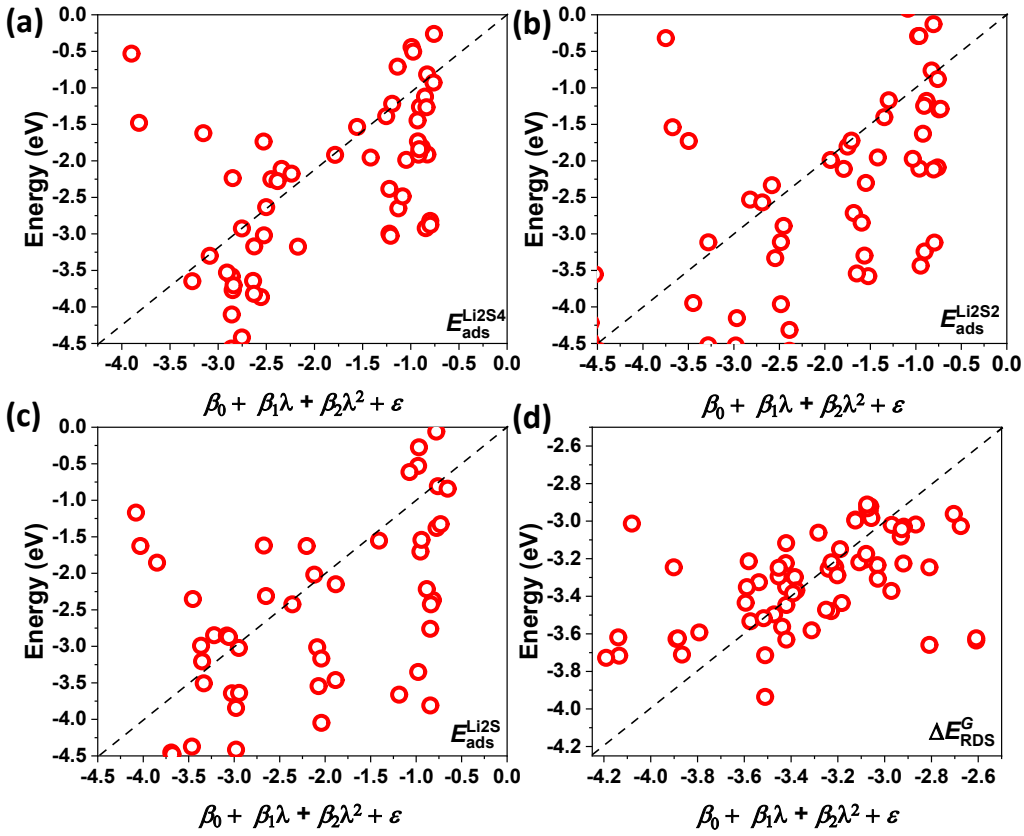

Supplementary Fig. 23 The fitting results of descriptor combinations ($\beta_0 + \beta_1\lambda + \beta_2\lambda^2 + \varepsilon$) obtained from quadratic polynomial regression with E_{ads}^{Li2S4} (a) , E_{ads}^{Li2S2} (b), E_{ads}^{Li2S} (c) *and* E_{RDS}^{G}(d).

$\lambda \in \left\{ \varepsilon_{d}^{spin\_up}, \varepsilon_{d}^{spin\_down}, 1/\varepsilon_{p}^{spin\_up}, 1/\varepsilon_{p}^{spin\_down} \right\}$

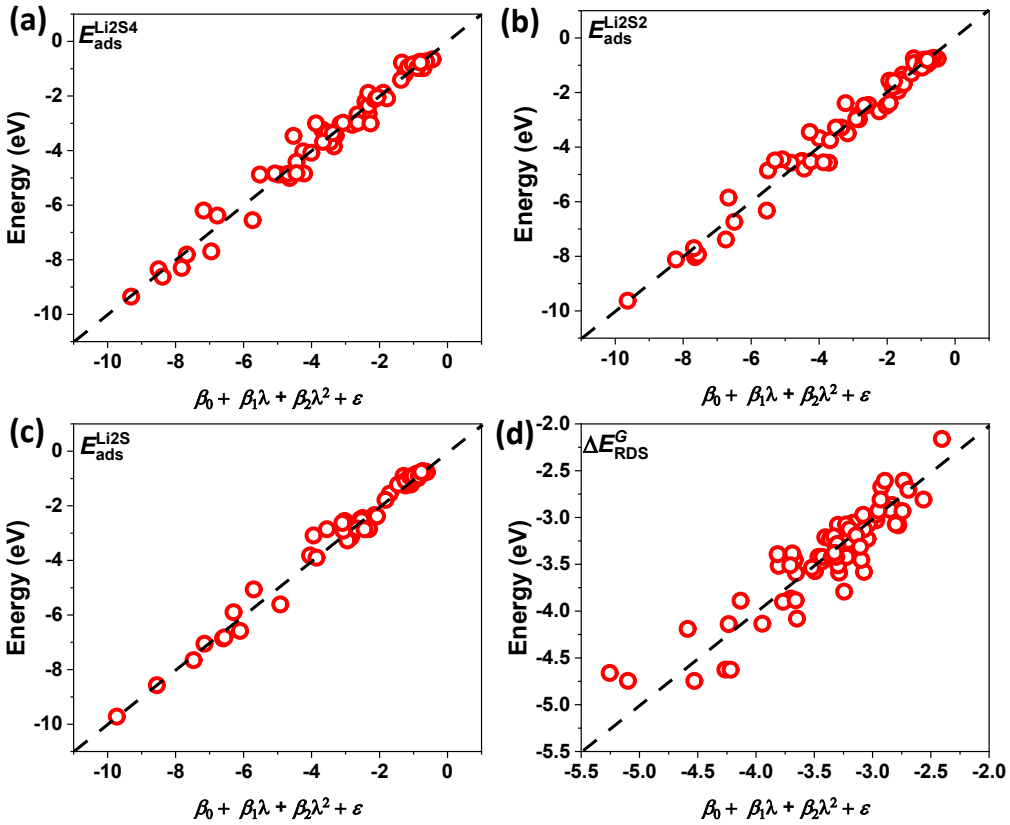

Supplementary Fig. 24 The fitting results of descriptor combinations ($\beta_0 + \beta_1\lambda + \beta_2\lambda^2 + \varepsilon$) obtained from quadratic polynomial regression with E_{ads}^{Li2S4} (a) , E_{ads}^{Li2S2} (b), E_{ads}^{Li2S} (c) *and* E_{RDS}^{G}(d).

$\lambda \in \left\{ \varepsilon_{d}^{spin\_up}, \varepsilon_{d}^{spin\_down}, 1/\varepsilon_{p}^{spin\_up}, 1/\varepsilon_{p}^{spin\_down}, \Delta E_{ion}, \Delta d, M_{ratio}, R_{ratio} \right\}$

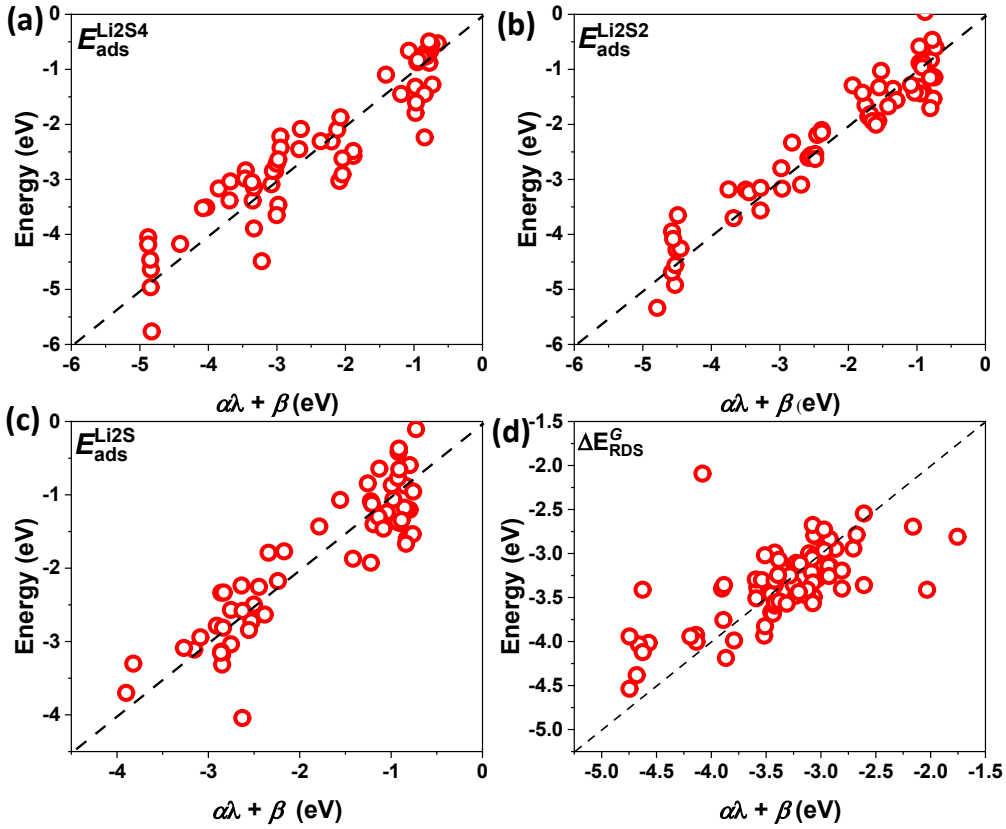

Supplementary Fig. 25 The fitting results of descriptor combinations (αλ + β) obtained from quadratic polynomial regression with E_{ads}^{Li2S4} (a), E_{ads}^{Li2S2} (b), E_{ads}^{Li2S} (c) *and* E_{RDS}^{G}(d).

$\lambda \in \left\{\varepsilon_{d}^{spin\_up}, \varepsilon_{d}^{spin\_down}, 1/\varepsilon_{p}^{spin\_up}, 1/\varepsilon_{p}^{spin\_down}\right\}$

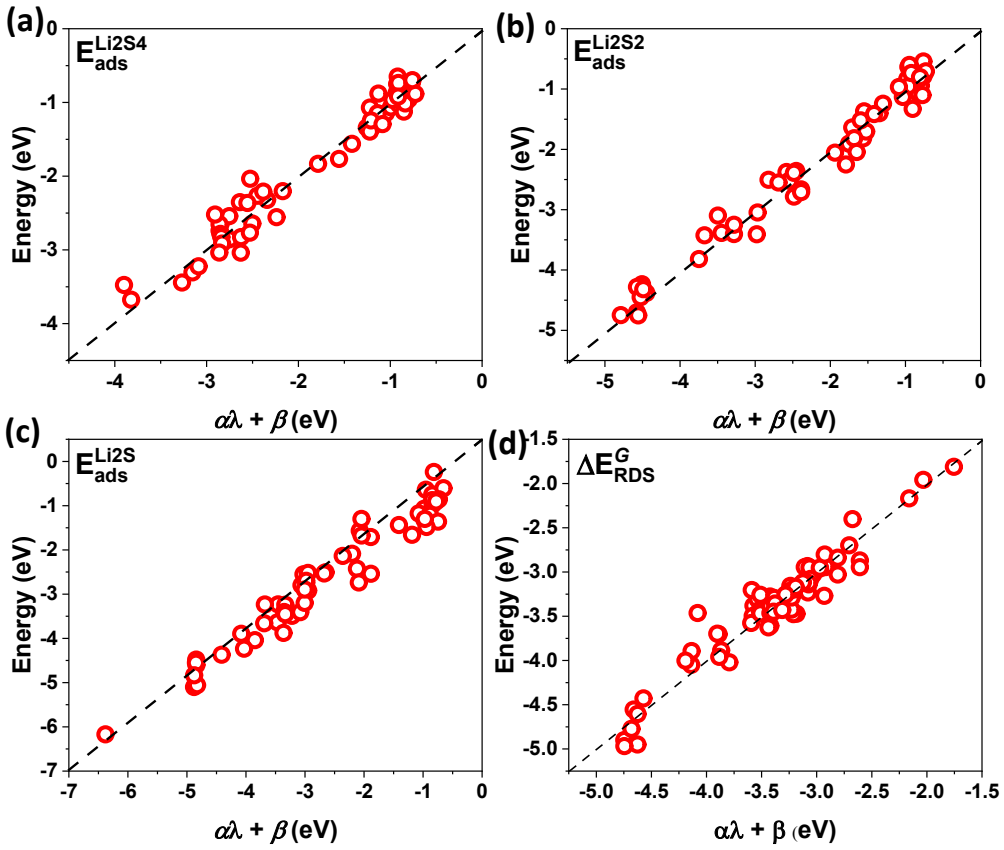

Supplementary Fig. 26 The fitting results of descriptor combinations ($\alpha\lambda + \beta$) obtained from quadratic polynomial regression with E_{ads}^{Li2S4} (a), E_{ads}^{Li2S2} (b), E_{ads}^{Li2S} (c) and E_{RDS}^{G}(d).

$\lambda \in \left\{\varepsilon_{d}^{spin\_up}, \varepsilon_{d}^{spin\_down}, 1/\varepsilon_{p}^{spin\_up}, 1/\varepsilon_{p}^{spin\_down}, \Delta E_{ion}, \Delta d, M_{ratio}, R_{ratio}\right\}$

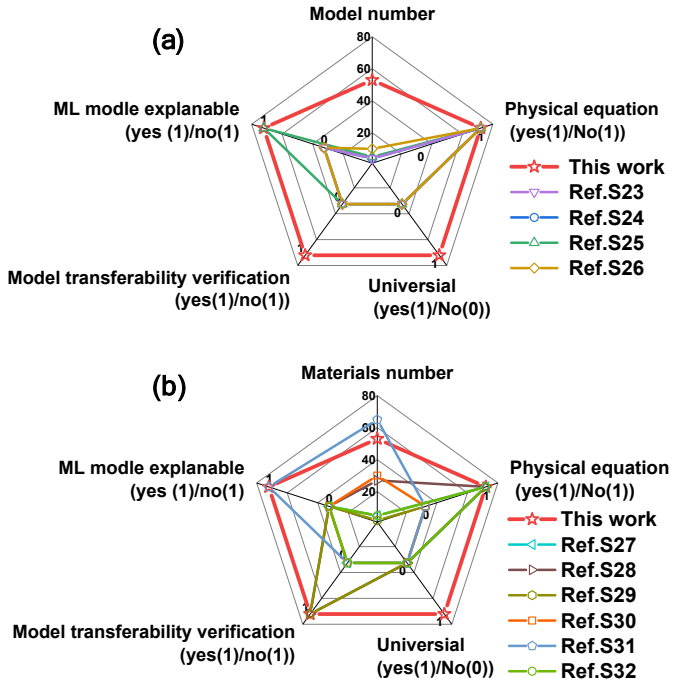

Supplementary Fig. 27 (a,b) Comparison of universality and transferability of the model constructed with the assistance of machine-learning algorithms in this work and the models reported in recent reports to describe the catalytic conversion kinetics of LPSs in Li-S batteries.

Supplementary Table 1. Comparing results of the uniqueness and generalizability of descriptors describing LPSs conversion kinetics in Li-S batteries between this work and recently published papers.

	This work	Ref.S24	Ref.S23	Ref.S25	Ref.S26	Ref.S27	Ref.S28	Ref.S29	Ref.S30	Ref.S31	Ref.S32
Materials_number	53	4	5	4	10	5	27	2	30	65	5
Physical_equation (yes (1)/no (0))	1	1	1	1	1	1	1	0	0	0	1
E_LPSs_binding (yes(1)/no(1))	1	1	1	0	1	0	1	1	1	1	0
E_Li_2S_decomposition (yes (1)/no (0))	1	0	1	0	1	0	0	0	0	0	0
LPSs_concersion_path (yes (1)/no (0))	1	1	0	0	1	0	1	0	0	0	0
Gibbs_energy_LPSs (yes (1)/no (0))	1	0	0	1	1	1	1	0	0	0	0
Model transferability verification (yes (1)/no (0))	1	0	0	0	0	0	1	1	0	0	0
ML_Algrithms_explanable (yes (1)/no (0))	1	-	1	-	-	-	-	0	0	1	-
ML_modle_explanable (yes (1)/no (0))	Quadratic polynomial algorithm	-	Solving coefficients	-	-	-	-	Neural Network	Neural Network	XGBoost	-
Physical equation	$\lambda = \varepsilon_d/\varepsilon_p$	ε_d	I(band), I(latt)	ε_d - ε_p	ε_d - ε_p	*p* charge	$\varepsilon_p + \chi_d$	-	-	-	*d*-states
Descriptors	$\beta_0+\beta_1\lambda+\beta_2\lambda^2$	ε_d	Genetic Algorithm + Monte Carlo Simulation	ε_d - ε_p	ε_d - ε_p	*p* charge	$\varepsilon_p + \chi_d$	-	-	-	t_{2g}

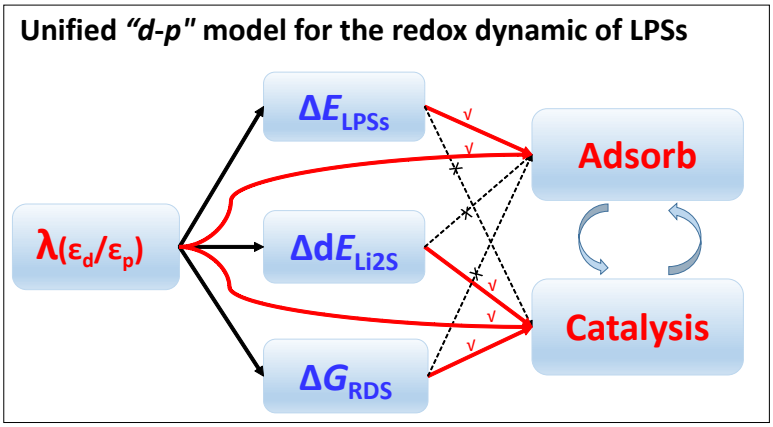

Supplementary Fig. 28 The diagram of λ unified describe three descriptors (ΔE_{LPSs}: Binding energy of LPSs; ΔdE_{Li2S}: the decomposition energy of Li_2S; ΔG_{RDS}: the Gibbs free energy change of rate-determined step) for uniformly describing the conversion of LPSs and also link the adsorption-catalysis process in the experiment.

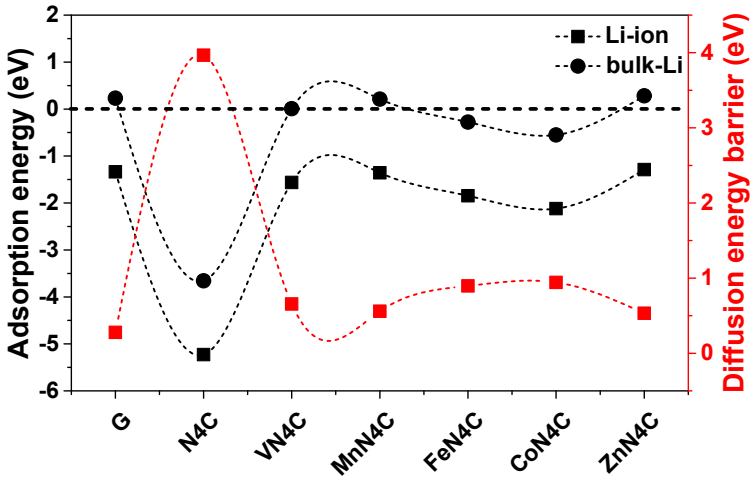

Supplementary Fig. 29 Li atom's adsorption energy and diffusion energy barrier on graphite, N_4C, and TMNCs (M =V, Mn, Fe, Co, and Zn) surfaces, respectively.

Finally, we also analyzed the binding effect of TMNCs toward Li atoms, as shown in Supplementary Fig. 18. By calculating the binding effects of G, N_4C, and TMNCs towards Li atoms, we found that higher binding energy corresponds lower Li diffusions dynamics along the surface. It indicates complex chemical conversion between lithium and TMNCs substrates like LPSs.

Supplementary noted 2: Experimental details and materials characterizations.

Synthesis of TMNCs (M = Fe, Co, V, and Mn) particles. In a typical synthesis of ZIF-8@$Fe(acac)_3$, $ZnNO_3$•$6H_2O$ (9.52g, 32mmol) and $Fe(acac)_3$ (0.113g, 0.32mmol or 1.13g, 3.2 mmol) were dissolved in a mixture solution of tetrahydrofuran (THF, 80mL) and methanol (160 mL) to form the clear solution A by ultrasound for 5 min at room temperature. Then 2-methylimidazole (10.512g, 0.11mol) was dissolved in a mixture solution of DMF (48 mL) and methanol (32 mL) to form solution B. Solution A and solution B were mixed and treated with ultrasound for 1~2 min, and then left undisturbed at 30 ^oC for 1-24h or transferred the mixture solution into the Teflon-lined autoclave at 120 ^oC for 4 h. The product was collected by centrifuging, washed with ethanol several times, and dried under vacuum at 70 ^oC for 8h. Similarly, the synthesis of other ZIF-8@M, just used the same molar of $Co(acac)_2$/$V(acac)_3$/$Mn(acac)_3$ to replace the $Fe(acac)_3$. Finally, the products were annealed at 1000 ^oC with a ramp rate of 3 ^oC min^{-1} for 3 hours in H_2/Ar flow to produce TMNCs.

Synthesis of the Li_2S_4/Li_2S_6/Li_2S_8 solution. According to previous reports[33], Li_2S_4 was synthesized via dissolving sulfur in super-hydride solution (1 M in THF) with a molar ratio of 2.75:1. The as-prepared solution was placed in the glovebox and dried naturally. Li_2S_4 powder was obtained by washing the precipitate with toluene solution and isolated by centrifuging. 0.33 M of the Li_2S_4 solution was prepared by dissolving the Li_2S_4 in Li-S electrolytes. 0.5 M of Li_2S_6 solution was synthesized by dissolving the

stoichiometric ratio of sulfur and lithium sulfide (Li_2S) (mole ratio of 5:1) in Li-S electrolytes. The Li_2S_8 solution (0.5M) was prepared by mixing sulfur and lithium sulfide (Li_2S) with a mole ratio of 7:1 in tetraglyme.

XANES and XAFS Characterizations. Before the analysis at the beamline, samples were pressed into thin sheets of 1 cm in diameter and sealed using Kapton tape film. The XAFS spectra were recorded at room temperature using a 4-channel Silicon Drift Detector (SDD) Bruker 5040. Fe K-edge extended X-ray absorption fine structure (EXAFS) spectra were recorded in fluorescence mode. Negligible changes in the line-shape and peak position of Fe K-edge XANES spectra were observed between two scans taken for a specific sample. The EXAFS spectra of these standard samples (Fe-foil, FePC, Fe_2O_3, and Fe_3O_4) were recorded in transmission mode. The spectra were processed and analyzed by Athena and Artemis software[34]. The single-atom models used for generating the scattering path in Feff6 were optimized by DFT calculations. The Hama software performed the wavelet transformation of the data, and the κ and σ were set as 10 and 1, respectively[35,36].

***In-situ* XRD characterization.** Be metal was used as the observation window to obtain the best X-ray penetration effects. The self-supported FeCFs@S as the cathode was next to the window and tested in Li-S electrolytes. The test time of XRD is 8 min 30 s for each time, and the range of test angle is from 5^o-40^o.

Li_2S_6 visualized adsorption tests. The 60 mM of Li_2S_6 solution was prepared by diluting 2 ml of Li_2S_6 (0.5 M) to 17 mL with THF. The TMNCs were immersed in 4.0 mL of Li_2S_6 solution for 48h at room temperature.

Li_2S depositions tests. 25 uL of the Li_2S_8 solution was dropped onto the cathode side (FeCFs/CFs/NCFs), and 20 uL of Li-S electrolytes was dropped onto the lithium anode side. After galvanostatically discharging to 2.06 V at a current of 0.113 mA (1/50 C, 1C = 1675mAh g^{-1}), the cells were potentiostatically discharged at 2.05 V until the current was lower than 0.01 mA. The nucleation capacity was calculated by the integrated area of the plotted curve using Faraday's Law. And the nucleation equations used for fitting the nucleation model of Li_2S are as follows[37]:

1) Instantaneous nucleation (2DI): $\frac{j}{j_m} = \left(\frac{t}{t_m}\right)\{exp|\frac{t^2 - {t_m}^2}{2{t_m}^2}|\}$
2) Progressive nucleation (2DP): $\frac{j}{j_m} = \left(\frac{t}{t_m}\right)^2\{exp|\frac{-2(t^3 - {t_m}^3)}{3{t_m}^3}|\}$
3) Instantaneous nucleation (3DI) $\frac{j}{j_m} = \left(\frac{1.9542}{t/t_m}\right)^{1/2}\{1 - exp[1.2564(\frac{t}{t_m})]\}$
4) Progressive nucleation (3DP) $\frac{j}{j_m} = \left(\frac{1.2254}{t/t_m}\right)^{1/2}\{1 - exp[2.3367(\frac{t}{t_m})^2]\}$

The thermodynamics properties of Li/S_8/Li_2S.

Supplementary Table 2. The Δ_fH_m, Δ_fS_m, Δ_fG_m of Li, S_8 and Li_2S

	16Li (aq) +	S_8 (aq) →	$8Li_2S$ (s)
Δ_fH_m (kJ mol^{-1})	159.37	102.3	*-447**
Δ_fS_m (J mol^{-1} K^{-1})	138.77	430.98	*63**
Δ_fG_m (kJ mol^{-1})	126.66	49.63	-439.02

$\Delta_rG^{\theta}_m$ (kJ mol^{-1}) = -5588.3kJ mol^{-1} = -58.02 eV; E = 3.62 V

Noted: We regard the $\Delta_rG^{\theta}_m$ of the reaction of $Li^+ + e^- \rightarrow Li$ as zero and used the aqueous model of Li (aq) and S_8 (aq) to replace the gas model in the electrocatalytic reaction. *https://en.wikipedia.org/wiki/Lithium_sulfide.

Calculation process:

$\Delta_rH^{\theta}_m = 8\Delta_fH^{\theta}_m(Li_2S) - \Delta_fH^{\theta}_m(S_8) - 16\Delta_fH^{\theta}_m(Li)$

$=8 \times [-447(kJ\ mol^{-1})] - 102.3(kJ\ mol^{-1}) - 16 \times 159.37(kJ\ mol^{-1})$

$= -6228.22(kJ\ mol^{-1})$

$\Delta_rS^{\theta}_m = 8\Delta_fS^{\theta}_m(Li_2S) - \Delta_fS^{\theta}_m(S_8) - 16\Delta_fS^{\theta}_m(Li)$

$= 8 \times [63(kJ\ mol^{-1})] - 430.98(kJ\ mol^{-1}) - 8 \times 138.77(kJ\ mol^{-1})$

$= -2147.3(kJ\ mol^{-1})$

$\Delta rG^{\theta}_m = 8\Delta_fG^{\theta}_m(Li_2S) - \Delta_fG^{\theta}_m(S_8) - 16\Delta_fG^{\theta}_m(Li) = \Delta_rH^{\theta}_m - T\Delta_rS^{\theta}_m$

$= -6228.22\ (kJ\ mol^{-1}) - 298(K) \times -2147.3(kJ\ mol^{-1})$

$= -5588.3\ (kJ\ mol^{-1})$

$8\Delta_fG^{\theta}_m(Li_2S) - 16 \times 126.66(kJ\ mol^{-1}) - 49.63(kJ\ mol^{-1}) = -5588.3\ (kJ\ mol^{-1})$

$\Delta_fG^{\theta}_m\ (Li_2S) = -439.016\ (kJ\ mol^{-1})$

$\Delta_rG^{\theta}_m$ (kJ mol^{-1})=-5588.3 kJ mol^{-1} = nFE

E = -5588.3 kJ mol^{-1}/96500 C mol^{-1}×16 = 3.62V

Finite Element Analysis for lithium plating with deformation. The calculations were performed on COMSOL multiphysics® software, and the model consists of a positive porous electrode and separator. The NMC (622) and $LiPF_6$/EC: EMC (3:7) are used for the positive electrode and electrolyte, respectively. The total length and width of the model are 150 um and 100 um, respectively, and the height of three small protrusions is 40 um. Lithium metal is deposited while charging on the negative electrode according to $Li^+ + e^- \rightarrow Li$. The deformed geometry algorithms calculated the shape changes of the lithium anode. The calibration method of mesh size is general physics, and free triangular is further set for the mesh for the lithium metal anode.

Assembly and testing of liquid/solid-state Li-S batteries for TMCFs@S.

All the coin cells were assembled in an Ar-filled glovebox with O_2 and H_2O content below 0.1 ppm. The coin cells (CR-2025) used for electrochemical performance testing were assembled with lithium foil as the anode, Celgard-2325 as the separator, and 1 M bis(trifluoroethanesulfony)imide lithium (LiTFSI) dissolved in 1,3-dioxolane (DOL)/diethyl carbonate (DME) (1:1 in volume) containing 2.0 wt % $LiNO_3$ as the electrolyte. The sulfur loading of TMCFs@S used for comparison is about 1.5 mg cm^{-2}. The cells were tested with galvanostatic cycling on a battery test system (LAND CT2001A) in the voltage window from 1.7 to 2.8 V (vs. Li^+/Li). Cyclic voltammetry and EIS tests were carried out on Gamry Interface 1000. The solid-state Li-S batteries used the SPE instead: the $Al(OTF)_3$ was dissolved in DOL (anhydrous, 99.8 %, containing 75 ppm BHT stabilizer) and reached a concentration of 5 mM and then dropped into the cathode, which was diluted to 0.5 mM by adding LiTFSI/DOL solution (2 M). The separator was used as the support film to avoid direct contact between cathode and anode. After assembling the batteries, the batteries stood for 12 h at 30 ^oC

to make the SPE form completely. The galvanostatic cycling was tested within the voltage window from 0.5 to 3.0 V (vs. Li/Li^+) at 60 ^oC.

Assembly and testing of half cells/symmetric cells for FeCFs@Li.

The Coulombic efficiency test was evaluated in the coin cell (CR2032) with Li foil as the counter electrode and FeCFs or Cu foil as working electrodes. Symmetric cells were assembled with two identical FeCFs@Li electrodes with the lithium deposition amount of 8 mAh cm^{-2}, and galvanostatic cycling in symmetric cells was conducted to evaluate the long-time cyclic stability. The Li-S battery electrolyte was served as the testing electrolyte.

Li-S Catalytic Kinetics Testing

EIS Testing at Different Discharge States: For new batteries, initiate with EIS testing; Discharge the battery to 2.4 V and conduct EIS testing; Discharge further to 2.1 V and perform EIS testing; Finally, discharge to 1.7 V and carry out EIS testing. Note: All tests should be conducted at the following temperatures: 283.15 K, 293.15 K, 303.15 K, 313.15 K, 323.15 K, and 333.15 K. For EIS tests, the frequency range should be from 10kHz to 0.1Hz. **Variable Rate CV (Cyclic Voltammetry) Test**: The CV (Cyclic Voltammetry) test ranges from 1.5V to 3.0V, with scan rates as follows: 0.05 mV s^{-1}, 0.1 mV s^{-1}, 0.2 mV s^{-1}, 0.5 mV s^{-1}, and 1 mV s^{-1}.

Supplementary Table 3. The atom ratio (%) calculated based on the EDX mapping data of the ZIF-8@M; the ZIF-8@M were synthesized with the molar ratio of Zn atoms and metal atoms is 10:1[a], and 100:1[b].

Materials[a]	C(%)	O(%)	M(%)
ZIF-8@Fe(acac)$_3$	93.21	6.28	0.51
ZIF-8@Co(acac)$_3$	99.45	5.05	0.50
ZIF-8@Mn(acac)$_3$	99.32	5.95	0.53
ZIF-8@V(acac)$_3$	97.34	2.19	0.47

Materials[b]	C(%)	N(%)	O(%)	M(%)
ZIF-8@Fe(acac)$_3$	71.29	24.14	4.38	0.19
ZIF-8@Co(acac)$_3$	66.89	29.46	3.47	0.18
ZIF-8@Mn(acac)$_3$	67.91	28.54	3.42	0.14
ZIF-8@V(acac)$_3$	68.89	29.03	1.93	0.14

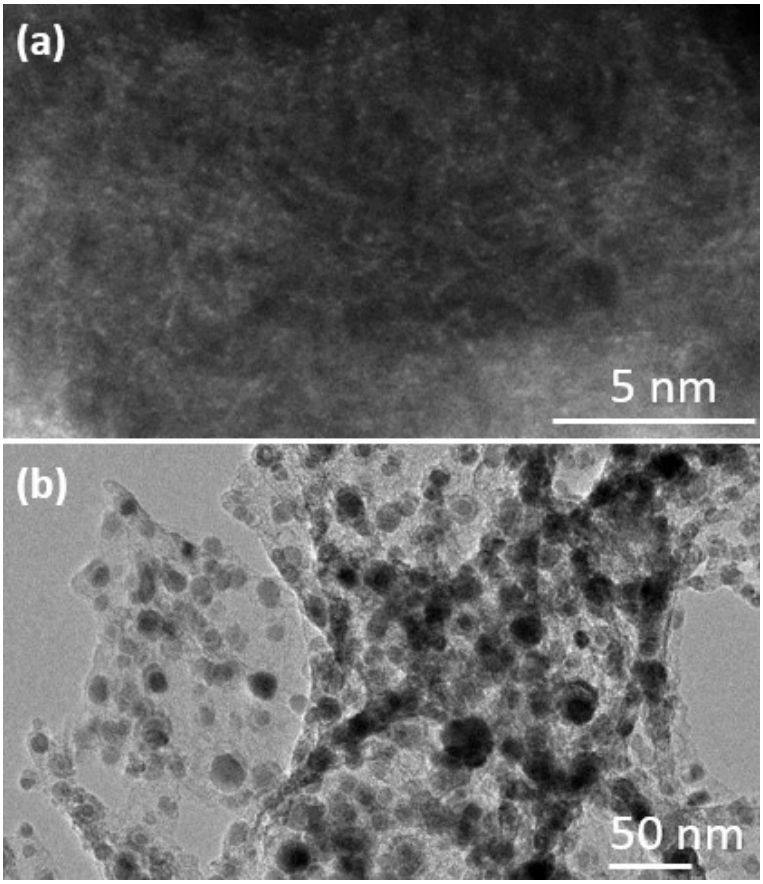

Supplementary Fig. 30 The HAADF-STEM images of FeNCs (a) and Fe_3C (b) materials.

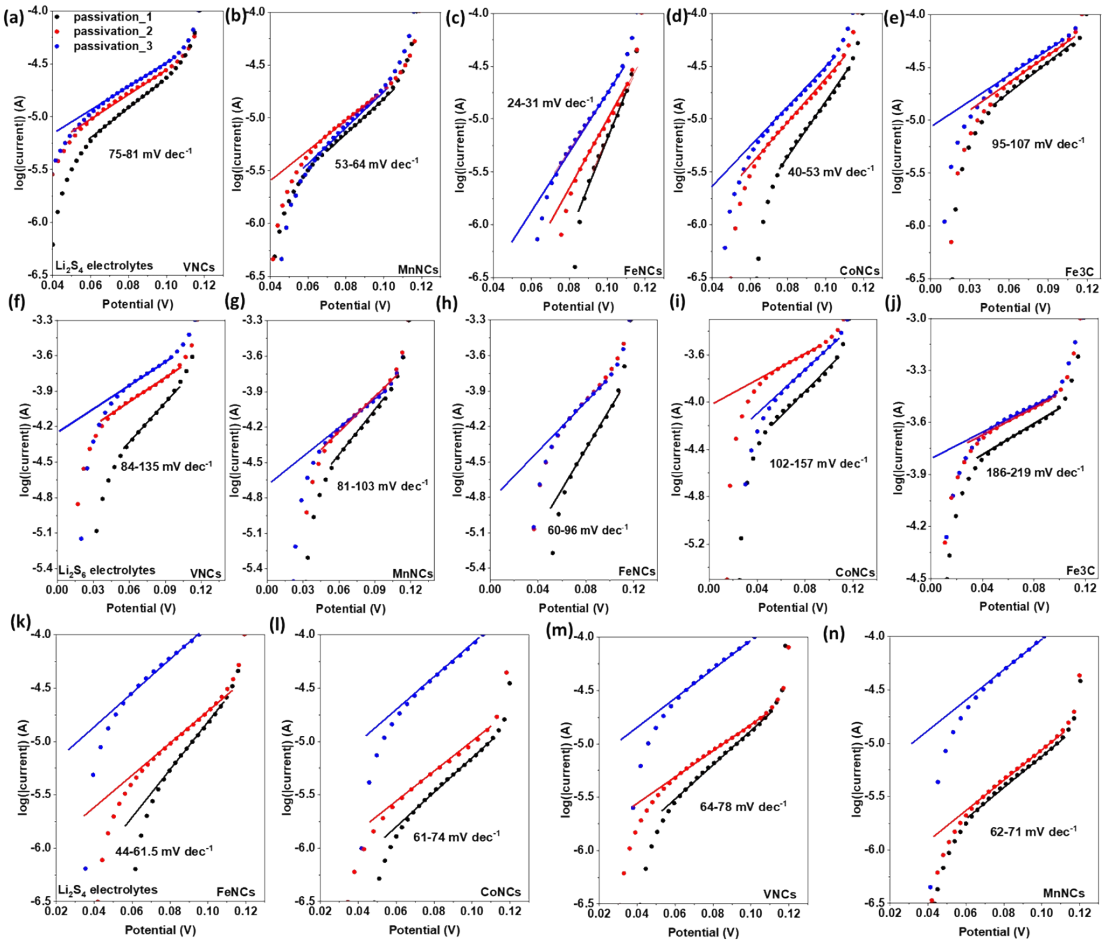

Supplementary Fig. 31 The conversion dynamics measurements of TMNCs and TMs (Fe_3C) catalysts in electrolytes containing the Li_2S_4/Li_2S_6. (**a-k**) The Tafel-slope fitting curve of VNCs (**a,f,k**), MnNCs (**b,g,l**), FeNCs (**c,h,m**), CoNCs (**d,l,n**), and Fe_3C (**e,j**), the measurements for (**a-e**) were conducted in electrolytes containing the Li_2S_4 and for the **(f-j)** were tested in electrolytes containing the Li_2S_6. **Noted:** the molar ratio of Zn atoms and metal atoms for the precursor ZIF-8@M used in (**a-j**) are 100:1, and for (**k-n**) are 10:1.

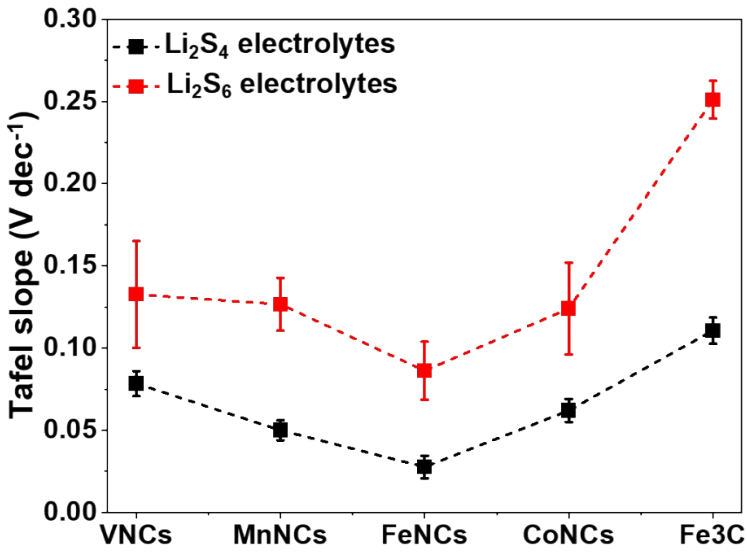

Supplementary Fig. 32 The Tafel slope of TMNCs tested in Li_2S_4/Li_2S_6 electrolytes with different passivation degrees.

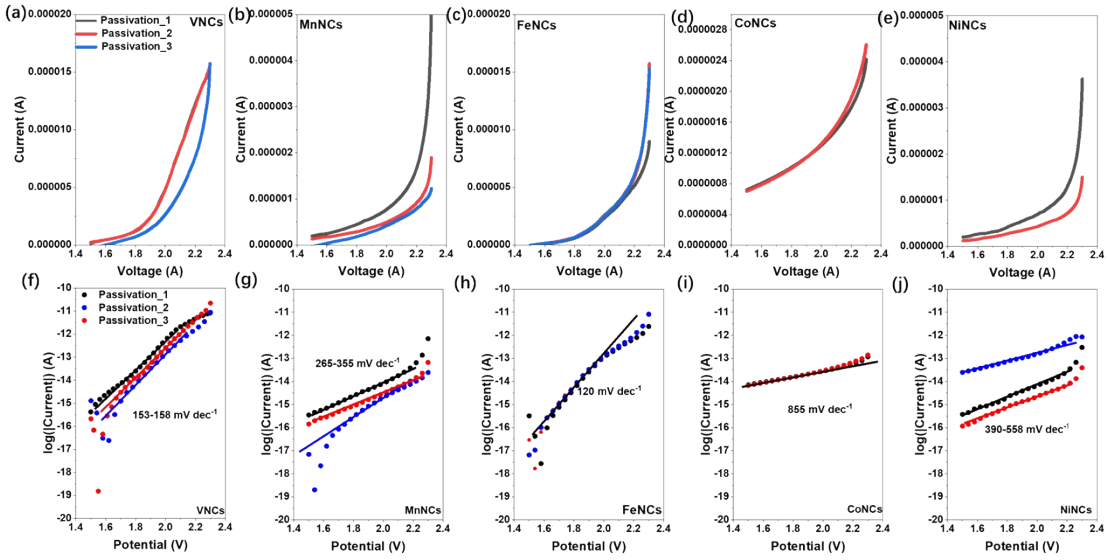

Supplementary Fig. 33 The conversion dynamics measurements of TMNCs catalysts in electrolytes containing the Li_2S_4. (**a-k**) The LSV curve and corresponding (**f-j**) Tafel curve of VNCs (**a**,**f**), MnNCs (**b**,**g**), FeNCs (**c**,**h**), CoNCs (**d**,**i**) and NiNCs (**e**,**j**);

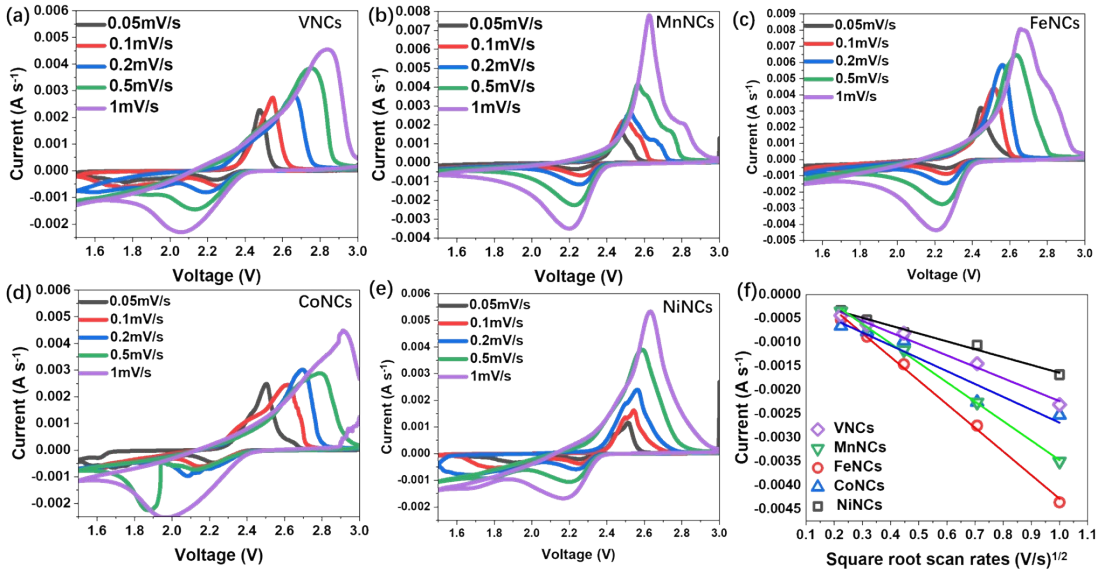

Supplementary Fig. 34 a-e, CV test results for VNCs(**a**), MnNCs(**b**), FeNCs(**c**), and CoNCs(**d**) and NiNCs(**e**) at 0.05, 0.1, 0.2, 0.5, and 1 mV s^{-1}; (**f**) the corresponding fitting data of CV peak value versus the square root of the scan rates ($v^{1/2}$).

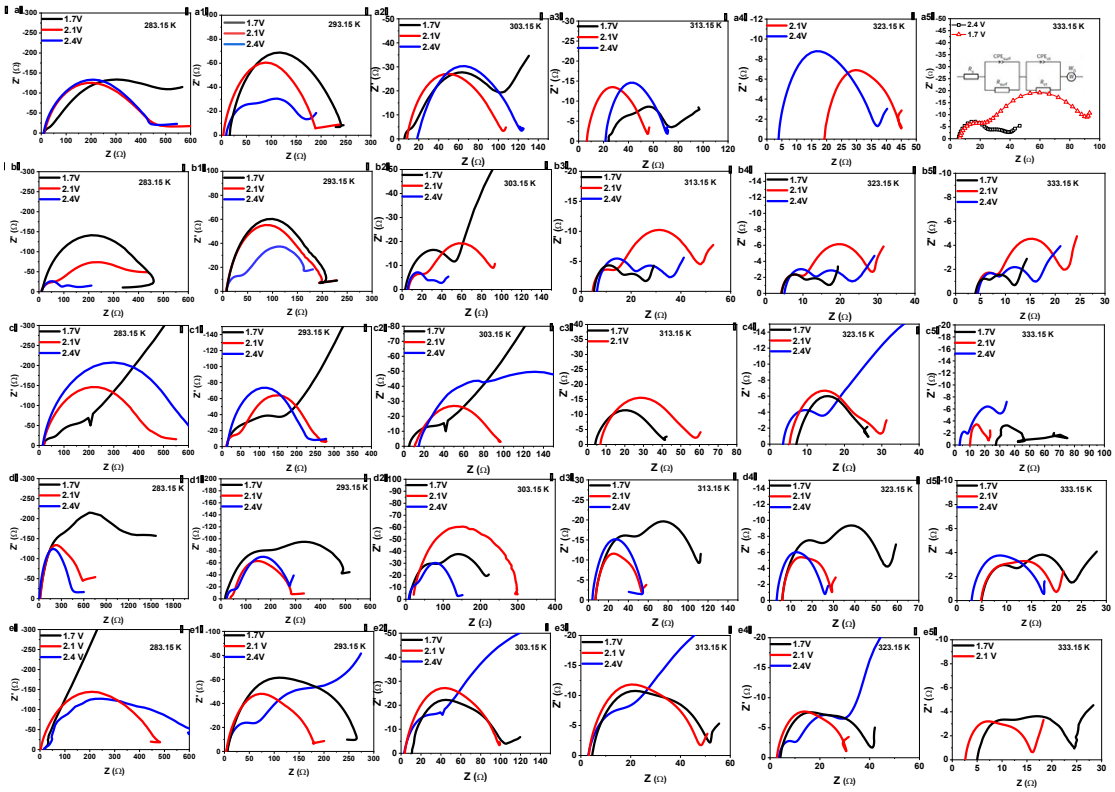

Supplementary Fig. 35 Nyquist plots of (**a-a1**) VNCs@S cathodes and (**b-b1**) MnNCs@S, (**c-c1**) FeNCs@S, (**d-d1**) CoNCs@S, (**e-e1**) NiNCs@S at different temperature and voltages. (**a-e**) 283.15 K; (**a1-e1**) 293.15 K; (**a2-e2**) 303.15 K; (**a3-e3**) 313.15 K; (**d4-e4**) 323.15 K; (**a5-e5**) 333.15 K.

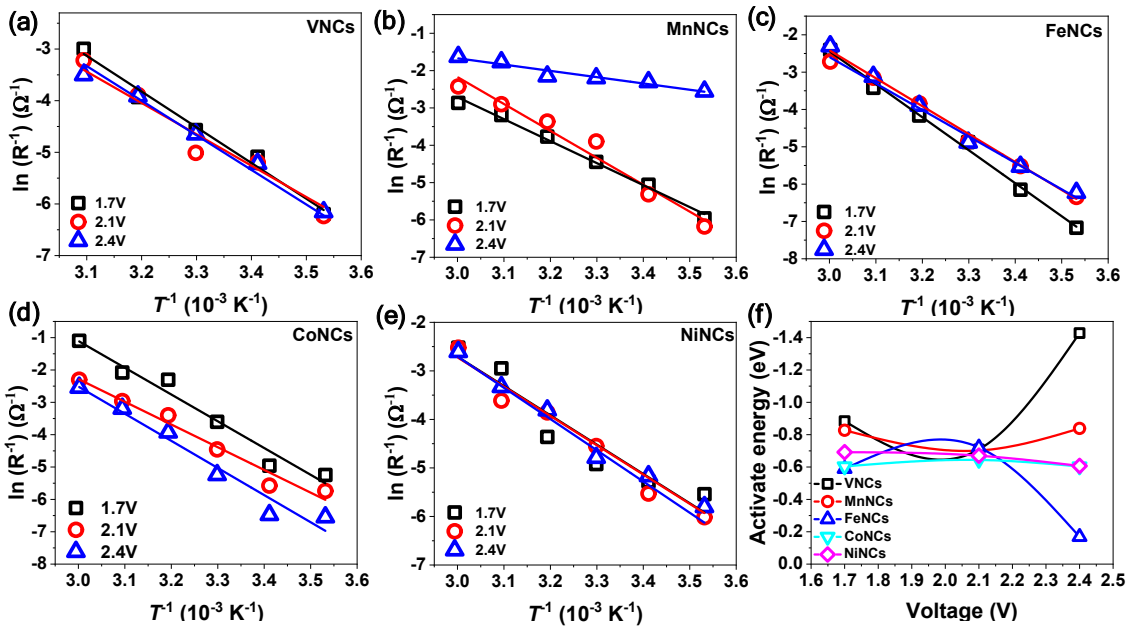

Supplementary Fig. 36 (a) Arrhenius plots for VNCs@S cathodes and (**b**) MnNCs@S, (**c**) FeNCs@S, (**d**) CoNCs@S, (**e**) NiNCs@S cathodes at varying voltages, where the reciprocal of the charge transfer resistance is employed to elucidate the rate of polysulfide conversion reactions. *T* denotes the absolute temperature, with linear fits of data points indicated by dashed lines, illustrates Nyquist plots at 2.4 V and 2.1 V at room temperature, alongside the equivalent circuit (inset) utilized for fitting the Electrochemical Impedance Spectroscopy (EIS) profiles. Z and Z represent the real and imaginary impedance, respectively. The elements within the circuit comprise: R_s, the combined internal resistance encompassing the interfacial contact resistance between the material and current collector, the ohmic resistance of the electrolyte, and the intrinsic resistance of the current collector; R_{surf}, surface resistance, attributed to the deposition of insoluble LiPS on the electrode surface; R_{ct}, the charge transfer resistance, representing the resistance of electrochemical reactions; CPE_{surf} and CPE_{ct} denote constant phase elements from surface deposition and charge transfer, respectively; W_0 is the Warburg impedance**. (f)** The activation energies of VNCs, MnNCs, FeNCs, CoNCs, and NiNCs at various voltages.

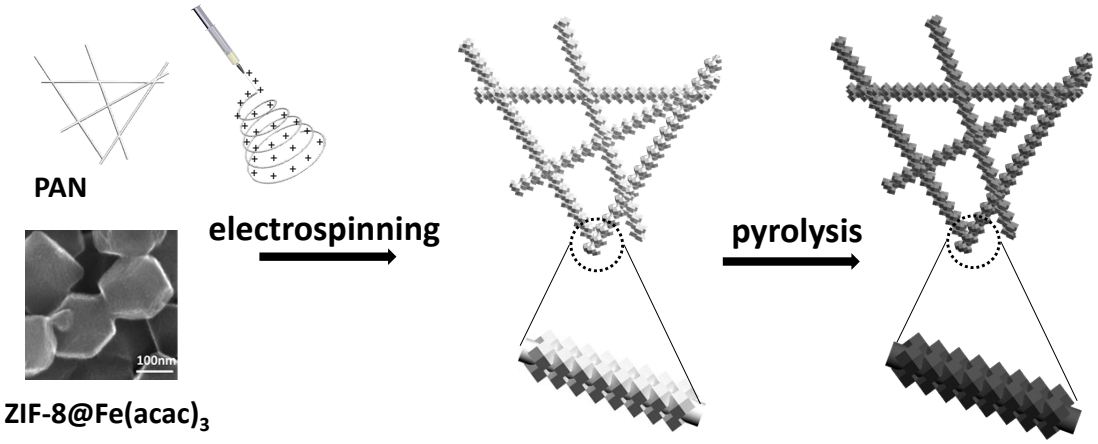

Supplementary Fig. 37 The scheme of the synthesized route for self-supported TMCFs (TM = V, Mn, Fe and Co).

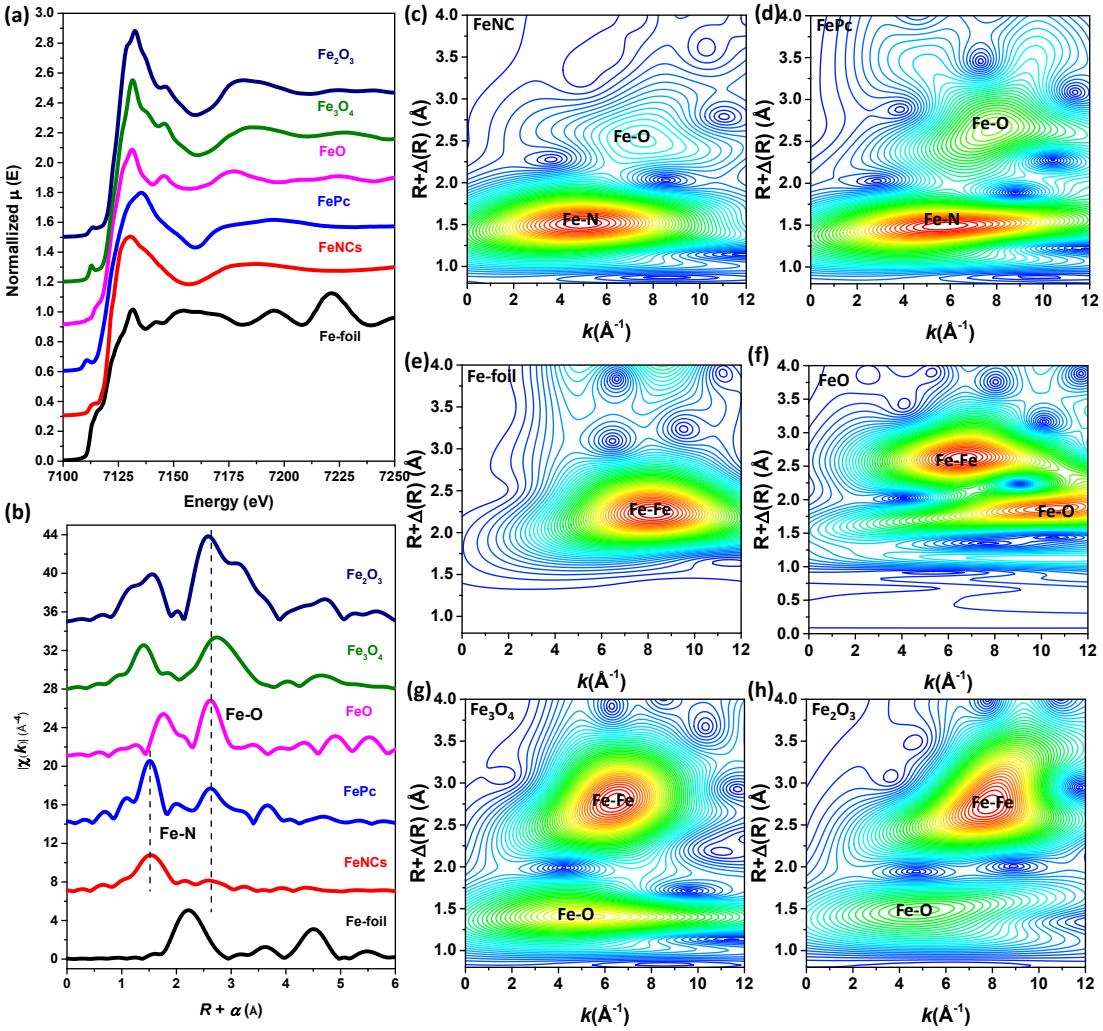

Supplementary Fig. 38 Structural characterizations of FeNCs by XANES and EXAFS measurements. (a) The experimental K-edge XANES spectra of FeNCs and reference samples (FePc, Fe-foil, FeO, Fe_3O_4, and Fe_2O_3). (**b**) The corresponding Fourier transformed magnitude of the experimental K-edge EXAFS signals in *R*-space. (**c-h**) Wavelet transforms for the k^3-weighted EXAFS signals of FeNCs and the reference samples.

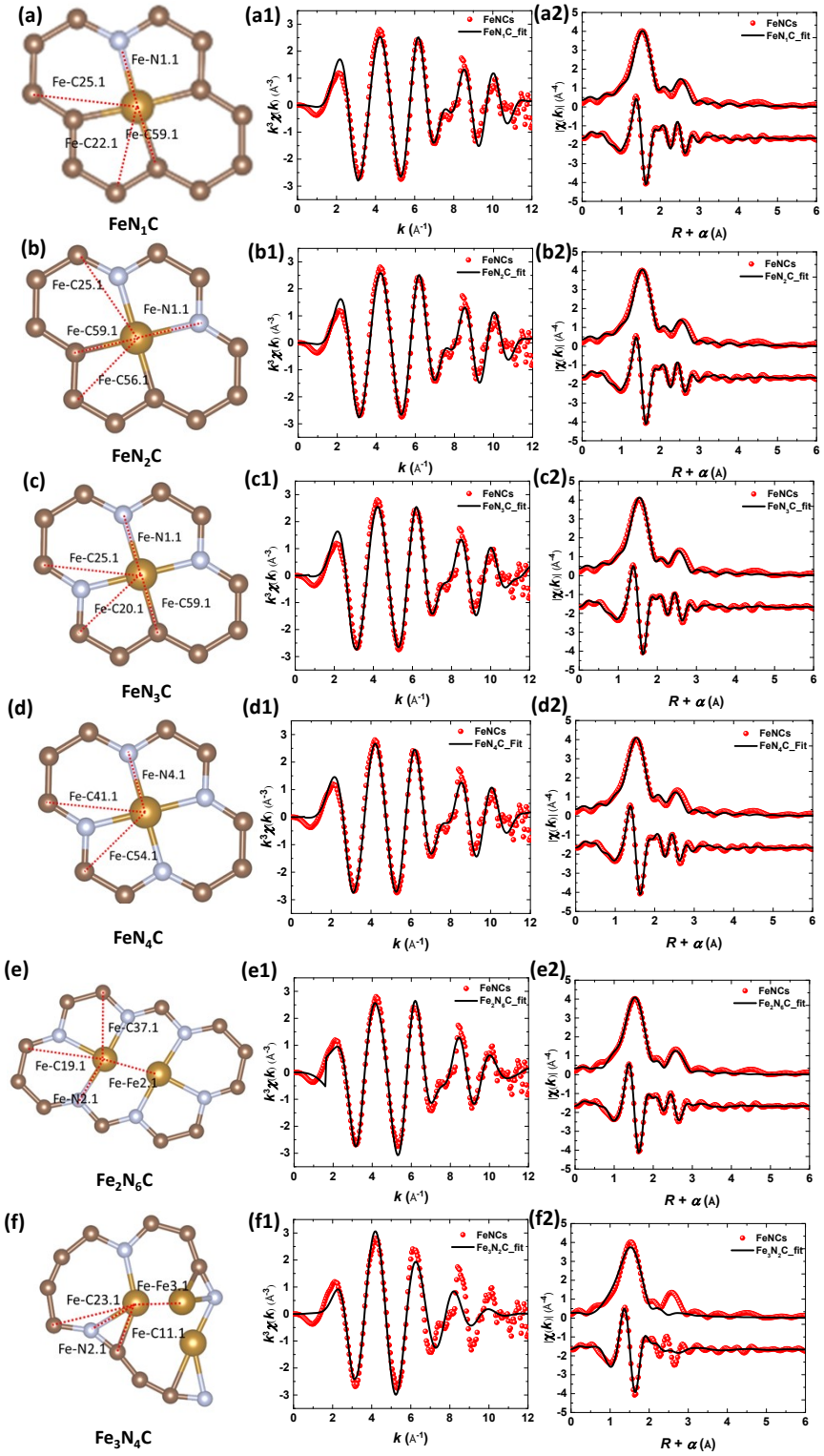

Supplementary Fig. 39 Fourier-transformed magnitude of Fe K-edge EXAFS spectra in *k*- and *R*-space. (a-f) The model of FeN_xC (x =1, 2, 3, 4), Fe_2N_6C, and Fe_3N_4C which were obtained from DFT calculation results. **(a1-f1)** The *k*-space data of EXFAS (points) and the curve-fit (line) of FeN_xC (x= 1, 2, 3, 4), Fe_2N_6C, and Fe_3N_4C model. (**a2-f2)** The corresponding *R*-space (FT-magnitude and imaginary component) data for EXFAS are k^3-weighted and not phase-corrected.

Supplementary Table 4 Curve fit Parameters[a] for Fe K-edge EXFAS for FeCFs samples based on FeN_4C model.

Path	d[b]/Å	N	R/Å	σ^2/Å
Fe-N4.1	1.905	4[c]	2.03(0.12)	0.009(0.002)[d]
Fe-C54.1	2.638	4[c]	2.67(0.02)	0.009(0.002)[d]
Fe-C41.1	3.041	4[c]	3.00(0.04)	0.009(0.002)[d]

[a]S_0^2 was about 0.95(0.11). ΔE_0 is the global fit parameter, returning a value of (2±1) eV. Data ranges: 2.5≤ k ≤10.5 Å-1, 1.0≤ R ≤3.0 Å. The number of variables is 7, out of a total of 9.9375 independent data points. R factors for this fit is 0.8%; [b]The distance for Fe-C4.1, Fe-C54.1, and Fe-N41.1 are from FEFF file of the FeN_4C model. The coordination numbers were constrained as [c]N(Fe-N4.1)=N(Fe-C54.1)=N(Fe-C41.1)=4 based on the crystal structure; [d]The Debye-Waller factors were constrained as σ^2(Fe-N4.1)=σ^2(Fe-N54.1)=σ^2(Fe-C41.1) for decreasing the correlation (or reducing the numbers of variables).

Supplementary Table 5 Curve fit Parameters[a] for Fe K-edge EXFAS for FeCFs samples based on FeN_1C mode.

Path	d[b]/Å	N	R/Å	σ^2/Å
Fe-C59.1	1.873	3[c]	2.06(0.19)	0.009(0.007)[d]
Fe-N1.1	1.986	1[c]	2.02(0.04)	0.009(0.007)[d]
Fe-C22.1	2.585	4[c]	2.67(0.09)	0.009(0.007)[d]
Fe-C25.1	3.068	4[c]	3.01(0.06)	0.009(0.007)[d]

[a]S_0^2 was about 1.05(0.64). ΔE_0 is the global fit parameter, returning a value of (0.4 ± 3) eV. Data ranges: 2.5≤k ≤10.5 Å^{-1}, 1.0≤ R ≤3.0 Å. The number of variables is 7, out of a total of 9.9375 independent data points. R factors for this fit is 1.2%; [b]The distance for Fe-C59.1, Fe-N1.1, Fe-C22.1, and Fe-C25.1 are from FEFF file of the FeN_4C model. The coordination numbers were constrained as N(Fe-C59.1)=3, N (Fe-N1.1)=1, and N(Fe-C22.1) = N(Fe-C25.1)=4 based on the crystal structure; [d]The Debye-Waller factors were constrained as σ^2(Fe-C59.1)=σ^2(Fe-N1.1)=σ^2(Fe-C22.1)=σ^2(Fe-C25.1) for decreasing the correlation (or reducing the numbers of variables).

Supplementary Table 6 Curve fit Parameters[a] for Fe K-edge EXFAS for FeCFs samples based on FeN_2C model.

Path	d[b]/Å	N	R/Å	σ^2/Å
Fe-C59.1	1.895	2[c]	2.06(0.16)	0.009(0.006)[d]
Fe-N1.1	1.937	2[c]	2.02(0.09)	0.009(0.006)[d]
Fe-C56.1	2.640	4[c]	2.67(0.03)	0.009(0.006)[d]
Fe-C25.1	3.061	4[c]	3.01(0.05)	0.009(0.006)[d]

[a]S_0^2 was about 1.02(0.25). ΔE_0 is the global fit parameter, returning a value of (0.3 ± 2) eV. Data ranges: 2.5≤ k ≤10.5 Å^{-1}, 1.0≤ R ≤3.0 Å. The number of variables is 7, out of a total of 9.9375 independent data points. R factors for this fit is 0.9%; [b]The distance for Fe-C59.1, Fe-C60.1, Fe-N1.1, and Fe-C22.1 are from FEFF file of the FeN_4C model. The coordination numbers were constrained as N(Fe-C59.1)=N (Fe-N1.1)=2 and N(Fe-C56.1) = N(Fe-C25.1)=4 based on the crystal structure; [d]The Debye-Waller factors were constrained as σ^2(Fe-C59.1)=σ^2(Fe-N1.1)=σ^2(Fe-C56.1)=σ^2(Fe-C25.1) for decreasing the correlation (or reducing the numbers of variables).

Supplementary Table 7 Curve fit Parameters[a] for Fe K-edge EXFAS for FeCFs samples based on FeN_3C model.

Path	d[b]/Å	N	R/Å	σ^2/Å
Fe-C59.1	1.875	1[c]	2.18(0.31)	0.008(0.002)[d]
Fe-N1.1	1.938	3[c]	2.02(0.09)	0.008(0.002)[d]
Fe-C20.1	2.660	4[c]	2.68(0.09)	0.008(0.002)[d]
Fe-C25.1	3.053	4[c]	3.03(0.02)	0.008(0.002)[d]

[a]S_0^2 was about 0.79(0.12). ΔE_0 is the global fit parameter, returning a value of (2 ± 1) eV. Data ranges: 2.5≤k ≤10.5 Å^{-1}, 1.0≤ R ≤3.0 Å. The number of variables is 7, out of a total of 9.9375 independent data points. R factors for this fit is 1.0%; [b]The distance for Fe-C59.1, Fe-C25.1, Fe-N1.1, and Fe-C20.1 are from FEFF file of the FeN_4C model. The coordination numbers were constrained as N(Fe-C59.1)=1, N (Fe-N1.1)=3, N(Fe-C20.1)=N(Fe-C25.1)=4 based on the crystal structure; [d]The Debye-Waller factors were constrained as σ^2(Fe-C59.1)=σ^2(Fe-N1.1)=σ^2(Fe-C20.1)=σ^2(Fe-C25.1) for decreasing the correlation (or reducing the numbers of variables).

Supplementary Table 8 Curve fit Parameters[a] for Fe K-edge EXFAS for FeCFs samples based on Fe_2N_6C model.

Path	d[b]/Å	N	R/Å	σ^2/Å
Fe-N2.1	1.921	3[c]	2.19(0.27)	0.014(0.002)[d]
Fe-Fe2.1	2.224	1[c]	2.05(0.17)	0.014(0.002)[d]
Fe-C37.1	2.645	3[c]	2.71(0.07)	0.014(0.002)[d]
Fe-C19.1	3.067	2[c]	3.08(0.02)	0.014(0.002)[d]

[a]S_0^2 was about 2.09(0.29). ΔE_0 is the global fit parameter, returning a value of (10 ± 2) eV. Data ranges: $2.5 \leq k \leq 10.5$ Å^{-1}, $1.0 \leq R \leq 3.0$ Å. The number of variables is 7, out of a total of 9.9375 independent data points. R factors for this fit is 1.0%; [b] The distance for Fe-N2.1, Fe-Fe2.1, Fe-C37.1, and Fe-C19.1 are from the optimized configuration of FeN_3C model via DFT calculations and the corresponding distance are from FEFF file of the Fe_2N_6C model. The coordination numbers were constrained as N(Fe-N2.1)=3, N (Fe-Fe2.1)=1, N(Fe-C37.1)=3, N(Fe-C19.1)=2 based on the crystal structure; [d] The Debye-Waller factors were constrained as σ^2(Fe-N2.1)=σ^2(Fe-Fe2.1)=σ^2(Fe-C37.1)=σ^2(Fe-C19.1) for decreasing the correlation (or reducing the numbers of variables).

Supplementary Table 9 Curve fit Parameters for Fe K-edge EXFAS for FeCFs samples based on Fe_3N_4C model.

Path	d[b]/Å	N	R/Å	σ^2/Å
Fe-C11.1	1.942	1[c]	2.13(0.19)	0.02(0.01)[d]
Fe-N2.1	1.951	2[c]	2.13(0.18)	0.02(0.01)[d]
Fe-Fe37.1	2.286	2[c]	2.04(0.23)	0.02(0.01)[d]
Fe-C23.1	3.152	4[c]	2.72(0.43)	0.02(0.01)[d]

[a]S_0^2 was about 2.00(4.12). ΔE_0 is the global fit parameter, returning a value of (1 ± 15) eV. Data ranges: $2.5 \leq k \leq 10.5$ Å^{-1}, $1.0 \leq R \leq 3.0$ Å. The number of variables is 7, out of a total of 9.9375 independent data points. R factors for this fit is 5%; [b]The distance for Fe-C11.1, Fe-N2.1, Fe-Fe37.1, and Fe-C23.1 are from the optimized configuration of FeN_3C model via DFT calculations and the corresponding distance are from FEFF file of the Fe_2N_6C model. The coordination numbers were constrained as N(Fe-C11.1)=1, N (Fe-N2.1)=2, N(Fe-Fe37.1)=2, N(Fe-C23.1)=4 based on the crystal structure; [d] The Debye-Waller factors were constrained as σ^2(Fe-C11.1)=σ^2(Fe-N2.1)=σ^2(Fe-Fe37.1)=σ^2(Fe-C23.1) for decreasing the correlation (or reducing the numbers of variables).

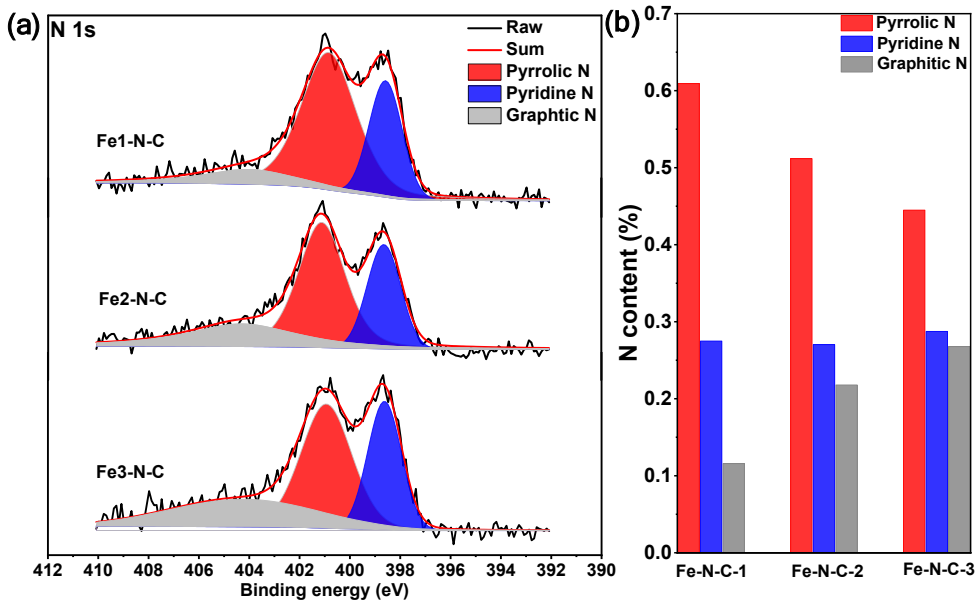

Supplementary Fig. 40 Characterization of N species in FeNCs samples containing different contents of Fe elements. (a) N1s XPS spectra; **(b)** the corresponding N contents of pyridine N, pyrrolic N, and graphitic N.

Supplementary Table 10 The ICP-MS results of FeNCs samples.

Number	m_0（g)	V_0（mL)	Elements	Content（%)
Fe-N-C-1	0.0145	25	Fe	0.17590%
Fe-N-C-2	0.0316	25	Fe	0.59194%
Fe-N-C-3	0.0218	25	Fe	1.37450%
Fe-N-C-4	0.0201	25	Fe	2.65330%

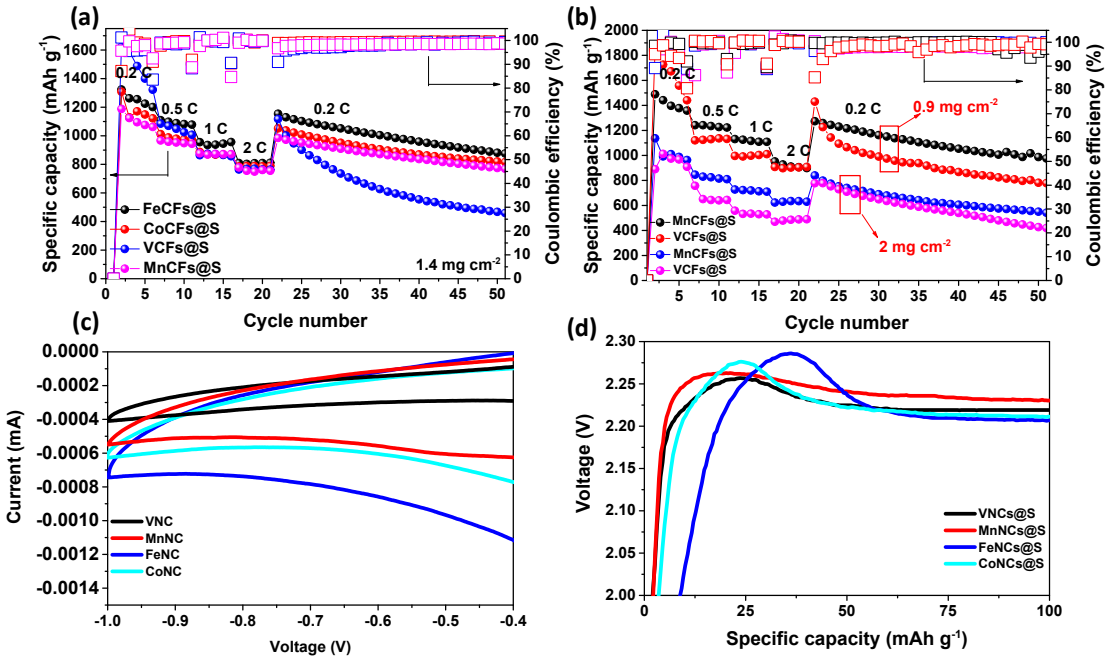

Supplementary Fig. 41 (**a**,**b**) Rate capability of Li-S batteries using TMCFs (VCFs, MnCFs, FeCFs, and CoCFs) as the sulfur hosts at different sulfur contents. (**c**) The CV curves were conducted in electrolytes containing the Li_2S_4. (**d**) The enlarged local area of the 2nd charge curve of TMCFs@S.

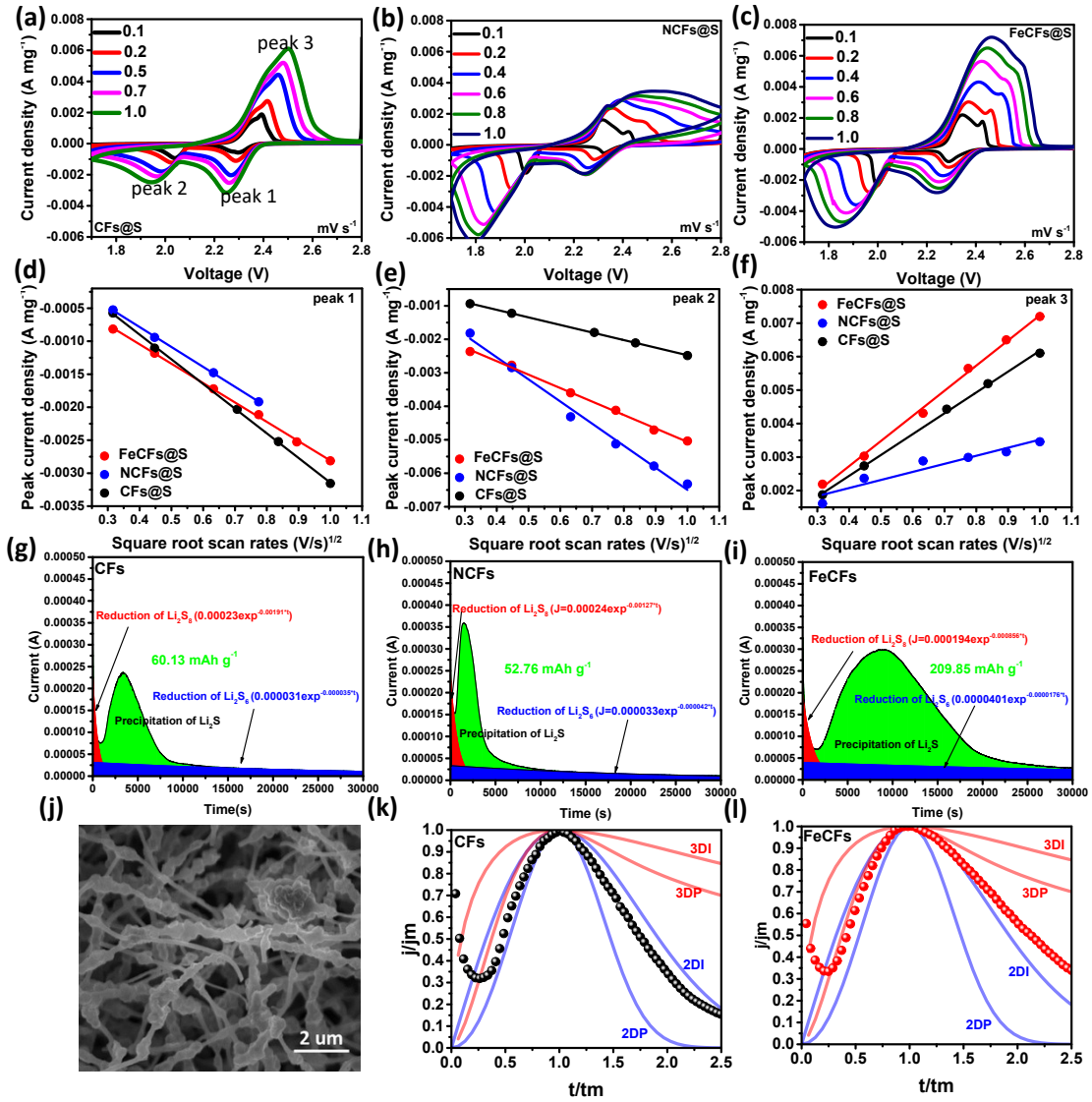

Supplementary Fig. 42 The CV curves and Li_2S deposition dynamics analysis of FeCFs, NCFs, and CFs in Li-S batteries. (a-c) The CV curves of CFs@S, NCFs@S, and FeCFs@S in Li-S batteries; **(d-f)** the corresponding fitting data of CV peak value versus the square root of the scan rates ($v^{1/2}$). **(g-i)** Potentiostatic discharge profiles of CFs, NCFs, and FeCFs in Li_2S_8 solution at 2.05 V and the corresponding curve fitting results. **(j)** SEM image of the Li_2S deposited on the FeCFs surface; **(k,l)** dimensionless current-time transient of CFs and FeCFs to perform peak fitting. j_m (peak current) and t_m (time needed to achieve the peak current) can be detected from the current-time transients.

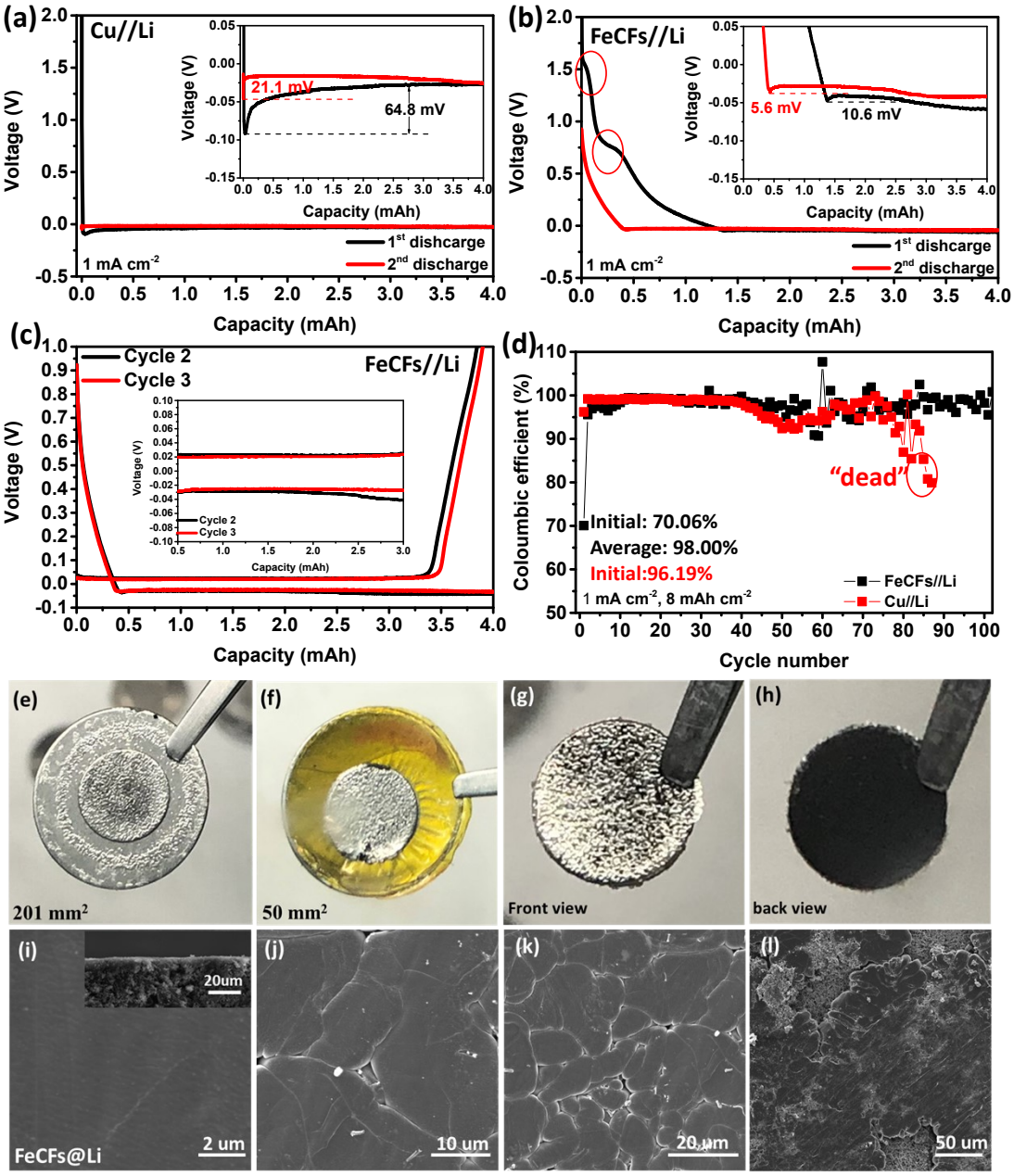

Supplementary Fig. 43 (a-c) The enlarged voltage profiles of Li plating/stripping on Cu (**a**) and FeCFs (**b,c**) substrates at a current density of 1.0 mA cm^{-2} with a fixed capacity of 1.0 mAh cm^{-2}; the inserts in (**a,b**) are the nucleation overpotential of Li-ion; and the inserts in **c** is the partial magnification graph. (**d**) The Coulombic efficiency profiles under 1 mAh cm^{-2} with a capacity of 8.0 mAh cm^{-2}. (**e-h**) The optical images of FeCFs@Li (deposited capacity: 8mAh cm^{-2}) with different depositing areas (50 mm^2 and 201mm^2). (**i-l**) Post-mortem SEM images of the FeCFs electrodes with 10 mAh cm^{-2} of Li deposited capacity in different magnifications.

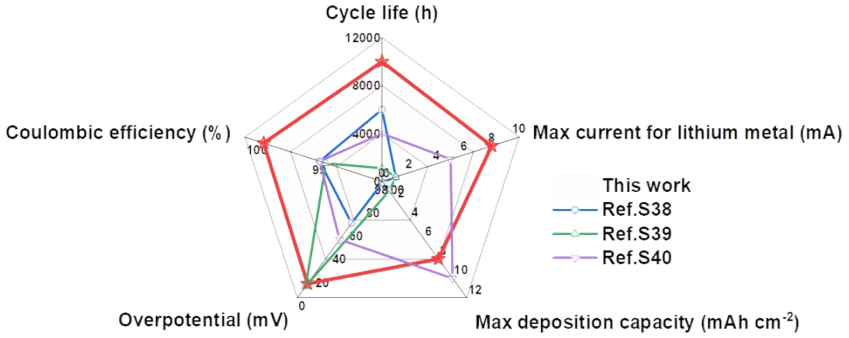

Supplementary Fig. 44 The electrochemical performance of solid-state Li-S batteries based on single-metal atom composite materials in this work is compared with the performance of metal single-atom materials reported in recent literature lithium-metal anodes.

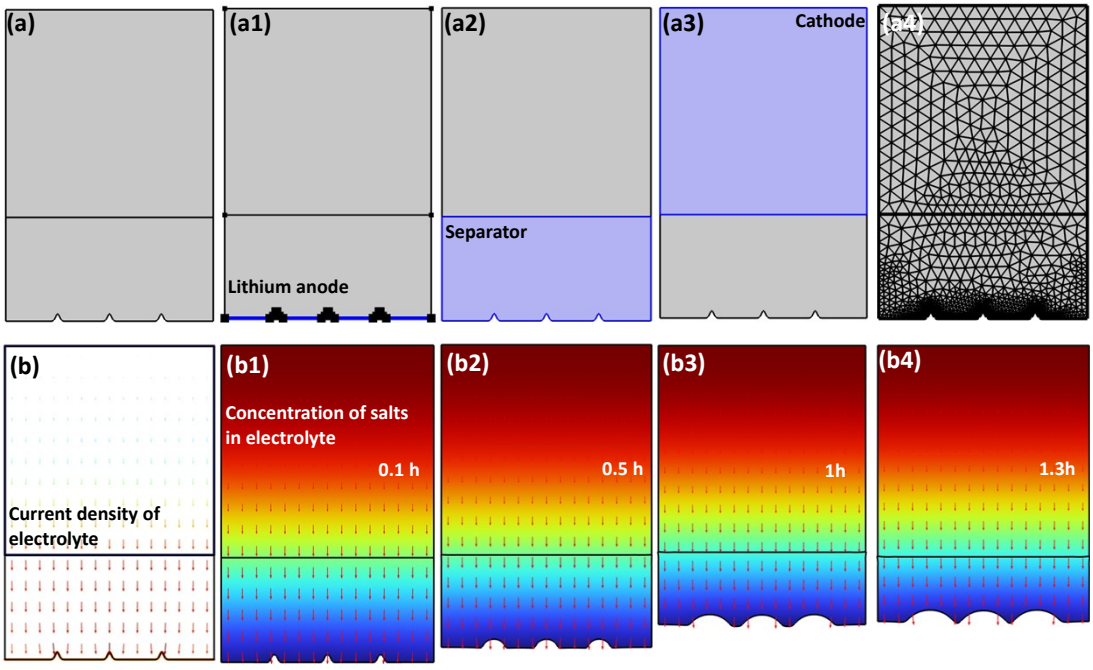

Supplementary Fig. 45 The finite element analysis for lithium plating with deformation. (a-a3) The composition of the calculation model for Li deposition: lithium anode (**a1**), separator (**a2**), and cathode (**a3**); (**a4**) the mesh density used for calculation. (**b-b4**) The calculation results of the current density of electrolytes (**b**) and the change of concentration of salts in electrolytes after calculating for 0.1h (**b1**), 0.5h (**b2**), 1h (**b3**), and 1.3h (**b4**).

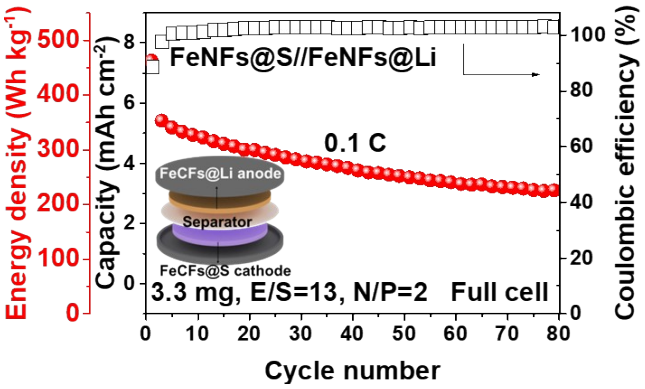

Supplementary Fig. 46 The performance of FeCFs@S//FeCFs@Li full cells: cycling stability at 0.1 C in liquid electrolytes.

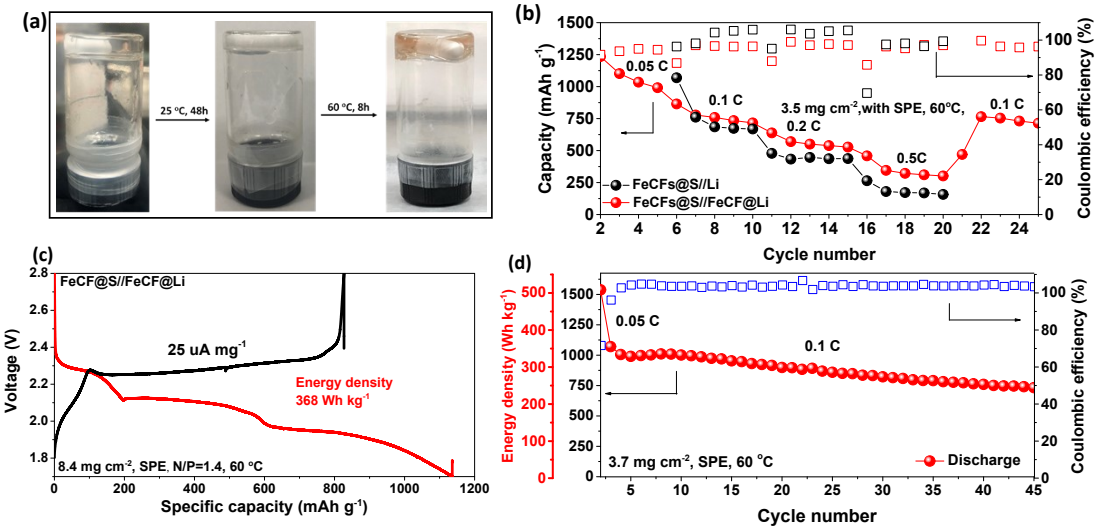

Supplementary Fig. 47 (a) The optical photos of pDOL at 30 °C for 48h and 60 °C for 8h, the yellow color appearing in electrolytes indicated the oxidation happened in pDOL. (**b)** The rate capability of Li-S half/full batteries in SPE. (**c**) discharge-charge voltage curves for 1st cycles at the current density of 25 uA mg^{-1} in SPE. (**d**) Cycling stability of FeCFs@S at 0.1 C in SPE.

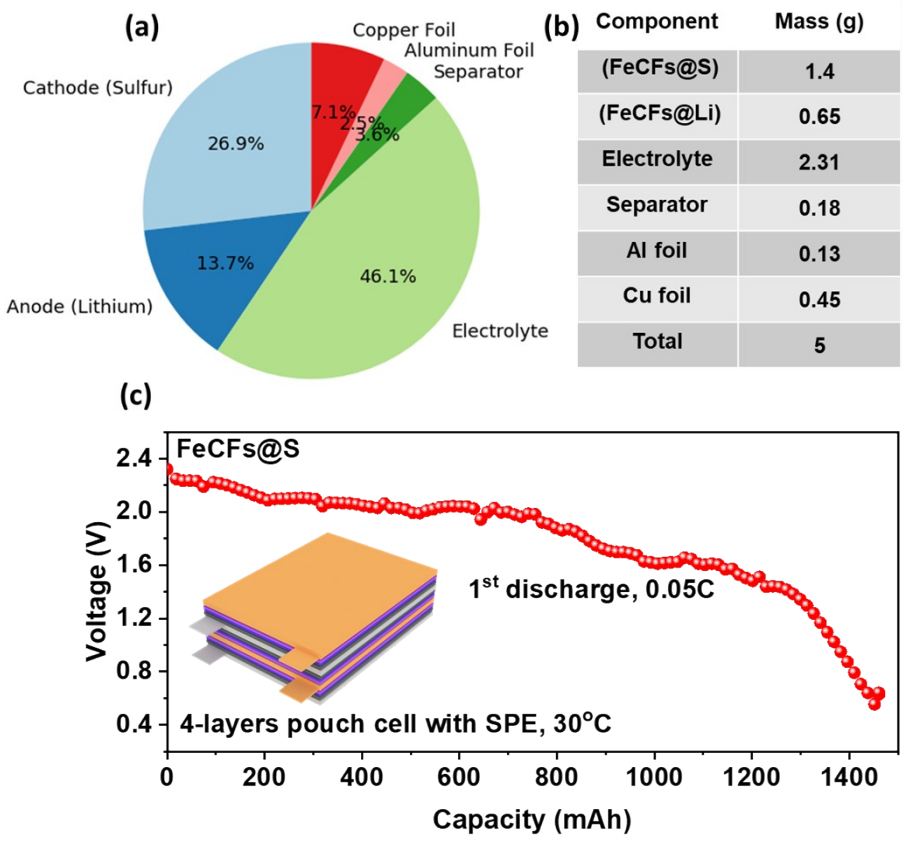

Supplementary Fig. 48 (**a**,**b**) The pie chart (**a**) of the mass ratio of each component in the battery and the detailed mass table (**b**). **c**, The capacity-voltage curve for the first discharge of 4-layers pouch.

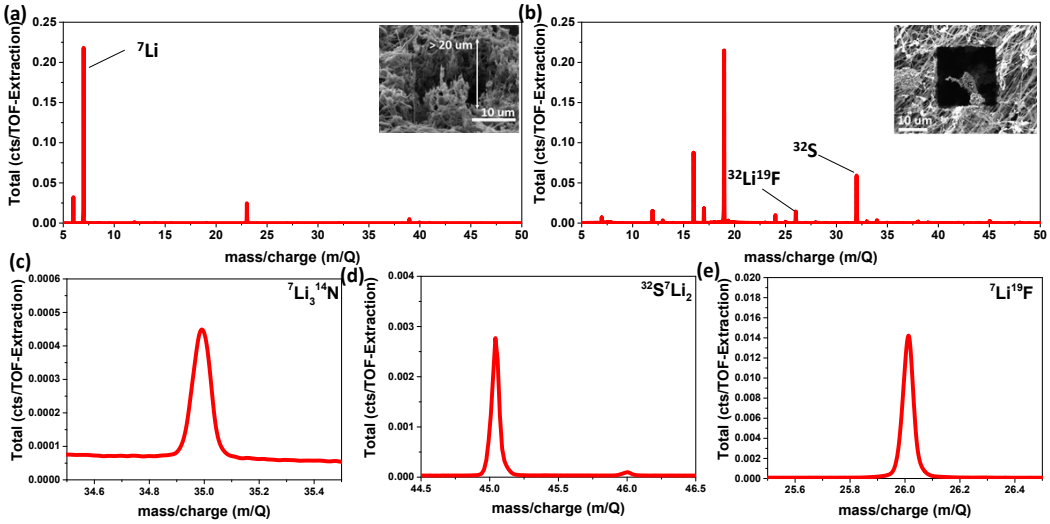

Supplementary Fig. 49 The ToF-SIMS results of cycled FeCFs@S (100 cycles, at the charge state). (**a**,**b**) The total spectrum were tested in positive mode (**a**) and negative mode (**b**), respectively. (The inserts in **a** and **b** are the SEM images of the sputtering area of the ToF-SIMs test.) (**c**-**e**) the enlarged curve of $Li_3{}^{14}N$ (c), $^{32}S^7Li_2$ (d), $^7Li^{19}F$ (e).

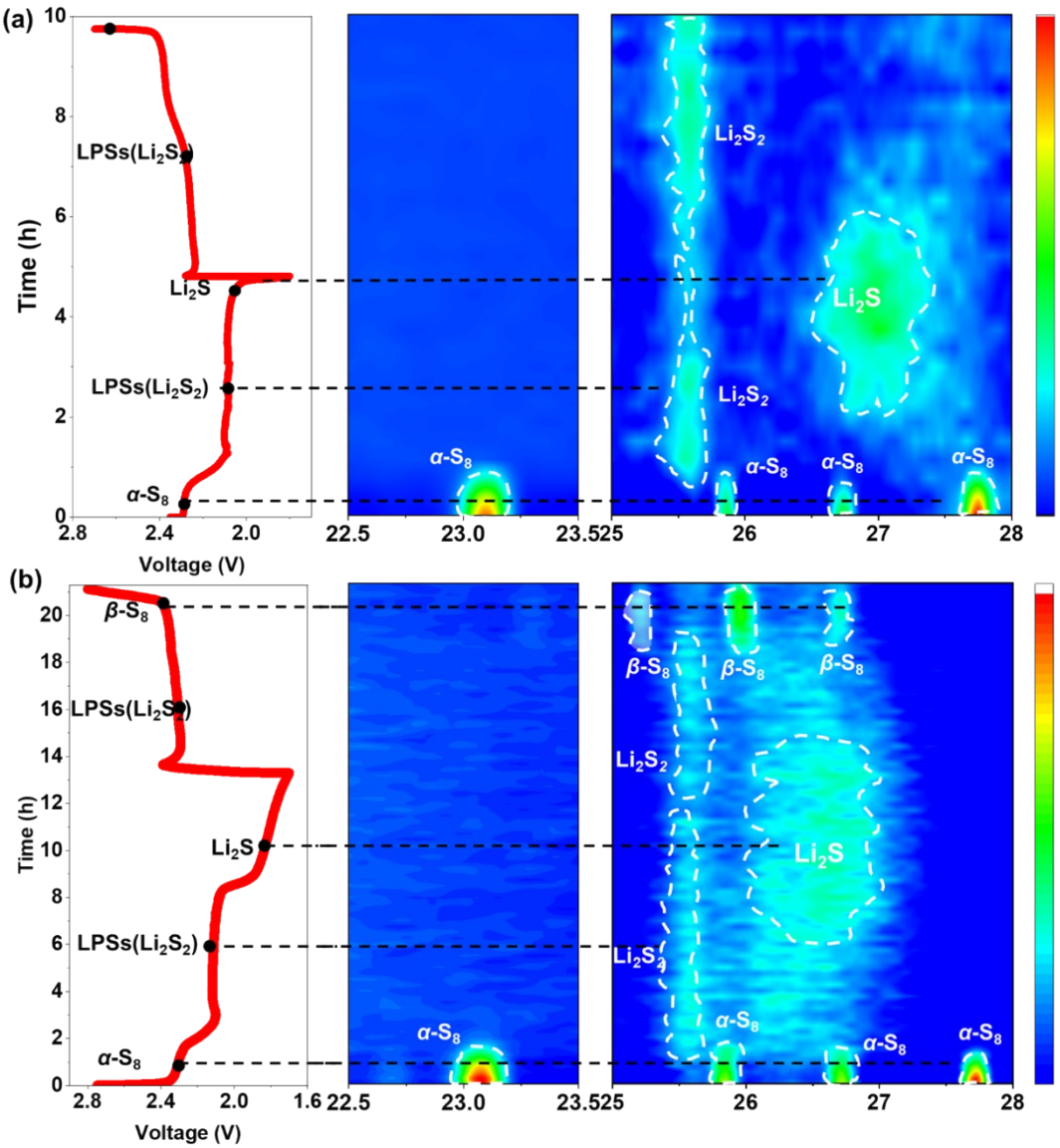

Supplementary Fig. 50 *In-situ* XRD measurement results of FeCFs@S and Fe_3C@LPSs in Li-S batteries. (a) The result of FeCFs@S tested at the current density of 0.5 C (sulfur loading: ~5 mg cm^{-2}). **(b)** The result of S@C with Fe_3C decorated separator tested at the current density of 0.1 C.

Movie S1. "AIMD-calculated Dynamic Adsorption of Polysulfides on Graphite Surface": This video presents a detailed AIMD (*ab-initio* Molecular Dynamics) simulation, showcasing the dynamic adsorption process of polysulfides on a graphite surface. The visualization highlights key molecular interactions and the structural changes of graphite under specific conditions, offering valuable insights into the material's behavior in real-world applications.

Movie S2. "AIMD-based Polysulfide Adsorption on Fe-Single-Atom with Tetra-N-Graphite surface": This video features an advanced AIMD simulation, focusing on the adsorption mechanism of polysulfides on a novel Fe-single-atom catalyst supported by a Tetra-N-Graphite surface. It provides an in-depth look at the molecular interactions and adsorption kinetics, illustrating the potential of this material in enhancing electrochemical performance.

Movie S3. "Dynamic Adsorption of Polysulfides on Tetra-N-coordinated Graphite Surface via AIMD": The video showcases a dynamic AIMD simulation of polysulfide adsorption on a Tetra-N-coordinated graphite surface. It highlights the unique interaction between polysulfides and the nitrogen-doped graphite, revealing insights into the efficiency and stability of this material in energy storage applications.

Movie S4. "In-situ TEM Observations of Structural Changes in Li-S Batteries with Li||Li_2O Solid Electrolyte during Discharge": This video provides an in-situ TEM (Transmission Electron Microscopy) observation of structural changes in lithium-sulfur (Li-S) batteries using a Li||Li_2O solid electrolyte during discharge. It offers a rare glimpse into the microscopic changes within the battery, elucidating the processes that occur during the discharge cycle and their implications for battery performance and longevity.

Supplementary References

1 G. Kresse and J. Furthmüller, *Phys. Rev. B*, 1996, **54**, 11169.

2 G. Kresse and D. Joubert, *Phys. Rev. B*, 1999, **59**, 1758.

3 J. P. Perdew, K. Burke and M. Ernzerhof, *Phys. Rev. Lett.*, 1996, **77**, 3865.

4 S. Grimme, J. Antony, S. Ehrlich and H. Krieg, *J. Chem. Phys.*, 2010, **132**, 154104.

5 G. Henkelman and H. Jónsson, *J. Chem. Phys.*, 2000, **113**, 9978.

6 K. Momma and F. Izumi, *J. Appl. Crystallogr.*, 2011, **44**, 1272.

7 V. Wang, N. Xu, J.-C. Liu, G. Tang and W.-T. Geng, *Comput. Phys. Commun.*, 2021, **267**, 108033.

8 S. L. Dudarev, G. A. Botton, S. Y. Savrasov, C. J. Humphreys and A. P. Sutton, *Phys. Rev. B*, 1998, **57**, 1505.

9 J. K. Norskov, S. Felix, A.-P. Frank and B. Thomas, *Fundamental Concepts in Heterogeneous Catalysis*, Wiley Press, 2014, 119. ISBN: 978–1–118-88895–7.

10 A. Logadottir, T.H. Rod, J.K. Nørskov, B. Hammer, S. Dahl, C.J.H. Jacobsen, *J. Catal.* 2001, **197**, 229.

11 G. Lippert, J. Hutter and M. Parrinello, *Mol. Phys.*, 1997, **92**, 477.

12 S. Goedecker, M. Teter and J. Hutter, *Phys. Rev. B*, 1996, **54**, 1703.

13 J. V. Vondele and J. Hutter, *J. Chem. Phys.*, 2007, **127**, 114105.

14 Y. A. Wang, *Chem. Phys. Lett.*, 1997, **268**, 76.

15 M. E. Tuckerman, P. J. Ungar, T. Rosenvinge and M. L. Klein, *J. Phys. Chem.*, 1996, **100**, 12878.

16 W. Humphrey, A. Dalke and K. Schulten, *J. Mol. Graph.*, 1996, **14**, 33.

17 F. Pedregosa, G. Varoquaux, A. Gramfort, V. Michel, B. Thirion, O. Grisel, M. Blondel, P. Prettenhofer, R. Weiss and et al., *J. Mach. Learn Res.* 2011, **12** 2825.

18 R. Ouyang, S. Curtarolo, E. Ahmetcik, M. Scheffler, and L. M. Ghiringhelli, *Phys. Rev. Mater.* 2018, **2**, 083802.

19 Liang, W. Zhao, J. Shen, X. Xu and J. Liu, *Appl. Phys. Lett.*, 2022, **121**, 223904.

20 S. Vijay, et al., *Nat. Catal.*, 2021, **4**, 1024.

21 M. T. Greiner, et al., *Nat. Chem.*, 2018, **10**, 1008.

22 J. Shen, et al., *Adv. Energy Mater.*, 2021, **11**, 2100673.

23 J. Zhou, et al., *Joule*, 2018, **2**, 2681.

24 Z. Shen, X. Jin, J. Tian, M. Li, Y. Yuan, S. Zhang, S. Fang, X. Fan, W. Xu, H. Lu, J. Lu and H. Zhang, *Nat. Catal.*, 2022, **5**, 555.

25 Z. Han, R. Gao, T. Wang, S. Tao, Y. Jia, Z. Lao, M. Zhang, J. Zhou, C. Li, Z. Piao, X. Zhang and G. Zhou, *Nat. Catal.*, 2023, **6**, 1073.

26 N. Gong, X. Hu, T. Fang, C. Yang, T. Xie, W. Peng, Y. Li, F. Zhang and X. Fan, *Adv. Energy Mater.*, 2022, **12**, 2201530.

27 W. Hua, T. Shang, H. Li, Y. Sun, Y. Guo, J. Xia, C. Geng, Z. Hu, L. Peng, Z. Han, C. Zhang, W. Lv and Y. Wan, *Nat. Catal.*, 2023, **6**, 174.

28 M. Fang, J. Han, S. He, J.-C. Ren, S. Li and W. Liu, *J. Am. Chem. Soc.*, 2023, **145**, 12601.

29 H. Zhang, Z. Wang, J. Ren and J. Liu, *Energy Storage Mater.*, 2021, **35**, 88.

30 Z. Lian, M. Yang, F. Jan and B. Li, *J. Phys. Chem. Lett.*, 2021, **12**, 7053.

31 H. Zhang, Z. Wang, J. Cai, S. Wu and J. Li, *ACS Appl. Mater. Interfaces*, 2021, **13**, 53388.

32 Z. Chen, W. Lv, F. Kang and J. Li, *J. Phys. Chem. C*, 2019, **123**, 25025.

33 X. Wang, et al., *Energy Environ. Sci.*, 2016, **9**, 2533.

34 B. Ravel and M. Newville, *J. Synchrotron Radiat.*, 2005, **12**, 537.

35 H. Funke, A. C. Scheinost and M. Chukalina, *Phys. Rev. B*, 2005, **71**, 094110.

36 H. Funke, M. Chukalina and A. C. Scheinost, *J. Synchrotron Radiat.*, 2007, **14**, 426.

37 Z. Li, Y. Zhou, Y. Wang and Y. C. Lu, *Adv. Energy Mater.*, 2019, **9**, 1802207.

38 Y. Zhu, Z. Lao, M. Zhang, T. Hou, X. Xiao, Z. Piao, G. Lu, Z. Han, R. Gao, L. Nie, X. Wu, Y. Song, C. Ji, J. Wang and G. Zhou, *Nat. Commun.*, 2024, **15**, 3914.

39 Q. Yang, J. Cai, G. Li, R. Gao, Z. Han, J. Han, D. Liu, L. Song, Z. Shi, D. Wang, G. Wang, W. Zheng, G. Zhou and Y. Song, *Nat. Commun.*, 2024, **15**, 3231.

40 C.-L. Song, Z.-H. Li, L.-Y. Ma, M.-Z. Li, S. Huang, X.-J. Hong, Y.-P. Cai and Y.-Q. Lan, *ACS Nano*, 2021, **15**, 13436.